



# OCIO and BrO observations in the volcanic plume of Mt. Etna – implications on the chemistry of chlorine and bromine species in volcanic plumes

J. Gliß<sup>1,2,3</sup>, N. Bobrowski<sup>2</sup>, L. Vogel<sup>4,2</sup>, D. Pöhler<sup>2</sup>, and U. Platt<sup>2</sup>

<sup>1</sup>Norwegian Institute for Air Research (NILU), Kjeller, Norway

<sup>2</sup>Institute of Environmental Physics, Heidelberg, Germany

<sup>3</sup>Faculty of Mathematics and Natural Sciences, Department of Physics, University of Oslo (UiO), Oslo, Norway

<sup>4</sup>Earth Observation Science, Space Research Centre, Department of Physics and Astronomy, University of Leicester, United Kingdom

Correspondence to: J. Gliß (jonas.gliss@nilu.no)

Received: 20 August 2014 – Published in Atmos. Chem. Phys. Discuss.: 1 October 2014

Revised: 15 April 2015 – Accepted: 16 April 2015 – Published: 26 May 2015

**Abstract.** Spatial and temporal profiles of chlorine dioxide (OCIO), bromine monoxide (BrO) and sulfur dioxide (SO<sub>2</sub>) of the volcanic plume at Mt. Etna, Italy, were investigated in September 2012 using Multi-Axis Differential Optical Absorption Spectroscopy (MAX-DOAS). OCIO was detected in 119 individual measurements covering plume ages up to 6 min. BrO could be detected in 452 spectra up to 23 min downwind. The retrieved slant column densities (SCDs) reached maximum values of  $2.0 \times 10^{14}$  molecules cm<sup>-2</sup> (OCIO) and  $1.1 \times 10^{15}$  molecules cm<sup>-2</sup> (BrO).

Mean mixing ratios of BrO and OCIO were estimated assuming a circular plume cross section. Furthermore, ClO mixing ratios were derived directly from the BrO and OCIO-SCDs. Average abundances of  $\overline{\text{BrO}} = 1.35$  ppb,  $\overline{\text{OCIO}} = 300$  ppt and  $\overline{\text{ClO}} = 139$  ppt were found in the young plume (plume age  $\tau < 4$  min) with peak values of 2.7 ppb (BrO), 600 ppt (OCIO) and 235 ppt (ClO) respectively.

The chemical evolution of BrO and OCIO in the plume was investigated in great detail by analysing the OCIO/SO<sub>2</sub> and BrO/SO<sub>2</sub> ratios as a function of plume age  $\tau$ . A marked increase of both ratios was observed in the young plume ( $\tau < 142$  s) and a levelling off at larger plume ages showing mean SO<sub>2</sub> ratios of  $3.17 \times 10^{-5}$  (OCIO/SO<sub>2</sub>) and  $1.65 \times 10^{-4}$  (BrO/SO<sub>2</sub>). OCIO was less abundant in the plume compared to BrO with a mean OCIO/BrO ratio of 0.16 at plume ages exceeding 3 min.

A measurement performed in the early morning at low solar radiances revealed BrO/SO<sub>2</sub> and OCIO/SO<sub>2</sub> ratios increasing with time. This observation substantiates the importance of photochemistry regarding the formation of BrO and OCIO in volcanic plumes.

These findings support the current understanding of the underlying chemistry, namely, that BrO is formed in an autocatalytic, heterogeneous reaction mechanism (in literature often referred to as “bromine explosion”) and that OCIO is formed in the reaction of ClO with BrO.

These new findings, especially the very detailed observation of the BrO and OCIO formation in the young plume, were used to infer the prevailing Cl-atom concentrations in the plume. Relatively small values ranging from  $[\text{Cl}] = 2.5 \times 10^6$  cm<sup>-3</sup> (assuming 80 ppb background O<sub>3</sub>) to  $[\text{Cl}] = 2.0 \times 10^8$  cm<sup>-3</sup> (at 1 ppb O<sub>3</sub>) were calculated at plume ages of about 2 min. Based on these Cl abundances, a potential – chlorine-induced – depletion of tropospheric methane (CH<sub>4</sub>) in the plume was investigated. CH<sub>4</sub> lifetimes between 14 h (at 1 ppb O<sub>3</sub>) and 47 days (at 80 ppb O<sub>3</sub>) were derived. While these lifetimes are considerably shorter than the atmospheric lifetime of CH<sub>4</sub>, the impact of gaseous chlorine on the CH<sub>4</sub> budget in the plume environment should nevertheless be relatively small due to plume dispersion (decreasing Cl concentrations) and ongoing mixing of the plume with the surrounding atmosphere (replenishing O<sub>3</sub> and CH<sub>4</sub>).

In addition, all spectra were analysed for signatures of IO, OIO and OBrO. None of these species could be detected. Upper limits for IO/SO<sub>2</sub>, OIO/SO<sub>2</sub> and OBrO/SO<sub>2</sub> are  $1.8 \times 10^{-6}$ ,  $2.0 \times 10^{-5}$  and  $1.1 \times 10^{-5}$  respectively.

## 1 Introduction

In the past years, improved measurement techniques, especially remote sensing methods, gained importance for the study of the chemical composition of volcanic plumes.

In this study we present Multi-Axis Differential Optical Absorption Spectroscopy (MAX-DOAS) measurements (e.g. Hönninger et al., 2004) of the volcanic plume at Mt. Etna on Sicily, Italy, performed in September 2012. MAX-DOAS is an established method to simultaneously study a variety of chemical species in volcanic plumes by analysing scattered sunlight spectra. Furthermore, it is easily possible to monitor the volcanic emissions over a wide range of different plume ages, which is of particular importance for studies related to the chemical evolution of the emitted species. It is well known that volcanic gases can have significant impacts on atmosphere and climate both on local and global scales (e.g. acid rain, stratospheric sulfur aerosols; see e.g. Robock, 2000). Furthermore, the chemical composition of volcanic plumes – especially in the young plume – can give insights into the degassing behaviour of the magma and may even be related to the state of activity of the volcano (e.g. Donovan et al., 2014). In addition, the environment of volcanic plumes provides an unique possibility to study details of complex chemical reaction mechanisms related to atmospheric ozone/oxidant chemistry in the presence of reactive halogen species (RHS).

The focus of this article is with regard to the chemical evolution of volcanic halogens, especially on the formation of RHS (e.g. BrO, ClO, OCIO) from the primarily emitted species (e.g. HCl, HBr) and their evolution in the ageing plume. The scientific interest in volcanic RHS increased dramatically when large amounts of bromine monoxide (BrO) were detected in the plume of Soufrière Hills volcano, Montserrat (Bobrowski et al., 2003). Today, we have only gained a rough understanding of the chemical processes involved in the RHS formation in volcanic plumes and possible dependencies due to the presence of other species (e.g. ozone or nitrogen oxides). Especially the conversion of the emitted HCl into reactive chlorine is still poorly understood. This is both due to a lack of measurement data and the complexity of the chemical processes involved.

## 2 Halogens in volcanic plumes

### 2.1 Initial plume composition

The main constituents of volcanic plumes are H<sub>2</sub>O, CO<sub>2</sub> and sulfur gases (dominated by SO<sub>2</sub>, H<sub>2</sub>S). Apart from these species, volcanoes also emit a certain amount of halogen species which are mainly released in the rather unreactive form of hydrogen halides such as HCl, HF, HBr, HI (e.g. Carroll and Holloway, 1994; Francis et al., 1995; Gerlach, 2004) and which are largely dominated by the chlorine emissions (HCl). Pyle and Mather (2009) reviewed past measurements (~1980–2008) of arc-related volcanic halogen emissions around the globe and found that HCl emissions contribute most with an estimated flux of  $4.3 (\pm 1) \text{ Tg a}^{-1}$ . HBr and HI emissions are orders of magnitude smaller with fluxes of 5–15 and 0.5–2 Gg a<sup>-1</sup> respectively.

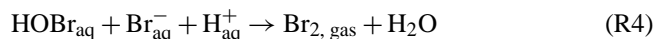
In the case of Mt. Etna, SO<sub>2</sub> / HCl ratios between 2 and 7 were found in past measurements (e.g. Francis et al., 1995; La Spina et al., 2010; Voigt et al., 2014). SO<sub>2</sub> appears to dominate the total sulfur emissions of Etna with SO<sub>2</sub> / H<sub>2</sub>S ratios of the order of 10<sup>1</sup>–10<sup>3</sup> (Jaeschke et al., 1982; Aiuppa et al., 2005).

A certain amount of the emitted hydrogen halides is converted into RHS, whereas the conversion from HBr into BrO appears to be much more efficient than the analogous reactions for volcanic chlorine. A key question related to these conversion mechanisms is the production of the halogen radicals (i.e. Br, Cl, I) in the plume. Once these are provided, oxidised halogens such as BrO and ClO are formed in reaction with ozone (O<sub>3</sub>).

### 2.2 Formation of RHS in the plume – the bromine explosion

A certain amount of RHS (e.g. Cl, Br) can be produced in the hot initial plume via high-temperature oxidative dissociation processes as suggested by model studies (e.g. Gerlach, 2004; Martin et al., 2006). Furthermore, Br can be formed via the reaction of HBr with OH in the very young plume (Roberts et al., 2009). However, the corresponding amounts are by far too small to explain the BrO amounts observed. In fact, the largest part of BrO is formed in atmospheric reactions, including the photolysis of Br<sub>2</sub> and BrCl (e.g. Oppenheimer et al., 2006; Bobrowski et al., 2007; Kern et al., 2009). This is further supported by direct observations showing a strong increase of the BrO levels in the young plume (e.g. Bobrowski et al., 2007; Bobrowski and Giuffrida, 2012) and the virtual absence during night-time (Kern et al., 2009). Nowadays, the underlying chemical reaction processes of the BrO formation in the young plume are mostly understood and likely driven by a heterogeneous and partly auto-catalytic reaction mechanism often referred to as “bromine explosion” (e.g. Lehrer et al., 1997; Wennberg, 1999), which includes the following reactions (note that the subscript “aq” denotes species in the

aqueous phase on particles).



The “bromine explosion” encompasses the uptake of hypobromous acid (HOBr) from the gas into the aqueous phase. After the reaction of HOBr with bromide,  $\text{Br}_2$  is released into the gas phase where it is rapidly photolysed, forming BrO in reaction with  $\text{O}_3$ . Once formed, the self-reaction of BrO induces a catalytic destruction of  $\text{O}_3$ . Noteworthy in this context are the similarities to observations of bromine emissions in polar regions (e.g. Barrie et al., 1988; Simpson et al., 2007). Measurements performed at Mt. Etna and Stromboli volcano (Aeolian islands, Italy) indicate that up to 11 % of the total emitted bromine is converted into BrO already within the first 5 min downwind (Wittmer et al., 2014).

### 2.3 Volcanic chlorine

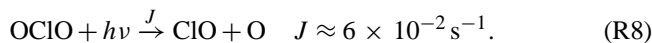
Potential formation processes of reactive chlorine species from the emitted HCl are still little studied. Apparently, the activation of chlorine is much weaker compared to bromine. This is indicated by the comparatively low Cl and  $\text{ClO}_y$  abundances we found (relative to the BrO ratios), indicating that less than 1 % of the emitted HCl is converted into reactive chlorine ( $\text{ClO}_y$ ) in the Etna plume. In other words,  $\text{ClO}_y / \text{HCl}$  is much smaller than  $\text{BrO} / \text{HBr}$ . In our opinion this phenomenon is mainly due to the fact that Br oxidation (conversion of bromide to Br, BrO) is a self-amplifying process (the bromine explosion) while Cl oxidation has no such properties. The reason why Br “explodes” but Cl does not is due to the relatively fast reaction of Cl atoms with  $\text{CH}_4$  (Platt and Janssen, 1995; Platt, 2000). Moreover, the dissolved chloride ions are less reactive compared to bromide ions (see Reaction R4) (von Glasow et al., 2009). Thus, Cl release is rather likely to be a by-product of the bromine explosion via formation of BrCl in the reaction of HOBr with chloride. However, the efficiency of this chlorine release channel strongly depends on the  $\text{Cl}^- / \text{Br}^-$  ion ratio in the condensed phase (Fickert et al., 1999). A significant release of BrCl is only likely for  $\text{Cl}^- / \text{Br}^-$  ratios exceeding  $10^4$ ; for instance a  $\text{Cl}^- / \text{Br}^-$  ratio of  $2 \times 10^4$  would yield a release of 50 % BrCl and 50 %  $\text{Br}_2$ . Direct sampling measurements at Mt. Etna revealed  $\text{Cl}^- / \text{Br}^-$  ratios of the order of  $10^2$  (Martin et al., 2008) up to  $10^3$  (Wittmer et al., 2014). For these values the HOBr uptake yields a release of more than 90 %  $\text{Br}_2$ . Note that this favoured  $\text{Br}_2$  release is probably even enhanced in

volcanic plumes due to the acid environment (low pH in the aerosol, for details see Fickert et al., 1999, i.e. the pH dependency of the discussed mechanisms). To our knowledge, there are no measurements indicating  $\text{Cl}^- / \text{Br}^-$  ratios of the order of  $10^4$  or larger at Mt. Etna. Hence, a significant BrCl release due to the HOBr uptake is relatively unlikely in the case of Mt. Etna.

Measurements of reactive chlorine species in volcanic plumes are still rare. Thus, the underlying chemistry is only partly understood and still bears large uncertainties, especially regarding the question of possible abundances of Cl atoms in the gaseous phase and the corresponding release mechanisms. However, once Cl atoms are provided, ClO is formed in the reaction with  $\text{O}_3$  and OCIO is then formed in the reaction of ClO with BrO:



The corresponding reaction rate coefficient is  $k_7 = 6 \times 10^{-12} \text{ cm}^3 \text{ s}^{-1}$  (at 298 K; Sander et al., 2006). Further possible reaction channels for the OCIO formation are orders of magnitude slower (e.g.  $\text{ClO} + \text{O}_3$ ,  $\text{ClO} + \text{ClO}$ ; Sander et al., 2006) and were not considered within this study. The main daytime sink of OCIO is its photolysis:



Both Bobrowski et al. (2007) and General et al. (2015) detected OCIO in the plume of Mt. Etna. The corresponding OCIO/ $\text{SO}_2$  ratios were between 3 and  $6 \times 10^{-5}$  (for spectra related to the plume centre). Simultaneous BrO measurements indicate an OCIO/BrO ratio of approximately 0.25 for Mt. Etna in both studies. Further detections of volcanic OCIO are reduced to satellite measurements (Puyehue-Cordón Caulle volcano, Chile) after an eruption in 2011 (Theys et al., 2014) and most recently the detection of OCIO in the plume of Soufrière Hills volcano (Montserrat) during a hiatus in 2011 (Donovan et al., 2014). In the latter study, comparatively large OCIO/ $\text{SO}_2$  ratios ( $4\text{--}6 \times 10^{-4}$ ) are reported as well as large OCIO/BrO ratios showing values up to 5 (i.e. about 20 times larger compared to Mt. Etna).

A key parameter for the OCIO formation in volcanic plumes is the prevailing availability of ClO and BrO molecules. Previous studies reported relatively large amounts of volcanic ClO measured with passive DOAS instruments (Bobrowski et al., 2007; Lee et al., 2005). The corresponding ClO/ $\text{SO}_2$  ratios were of the order of 5 % hence, almost 3 orders of magnitude more ClO than OCIO. However, these measurements have to be treated cautiously due to difficulties and uncertainties in the DOAS evaluation of ClO.

Furthermore, to our knowledge it has not yet been possible to reproduce these measurements in model studies (e.g. Bobrowski et al., 2007; von Glasow, 2010). Kern et al. (2009) investigated ClO and OCIO abundances at the vent

of Masaya Volcano (Nicaragua) using an active long-path DOAS instrument. They did not detect any of both species most likely due to the proximity of the measurement to the crater (i.e. early stage of the RHS formation). In addition, the halogen content of Masaya volcano is probably smaller compared to Mt. Etna (Pyle and Mather, 2009). While the OCIO / ClO ratios should typically be of the same order of magnitude in the case of Mt. Etna and Masaya (Kern et al., 2009; this study), this seems not to be the case for the Puyehue–Cordón Caulle eruption in 2011 which actually indicates a large excess of ClO compared to OCIO and even BrO (Theys et al., 2014).

The focus of this article is the temporal and spatial evolution of RHS in volcanic plumes (especially BrO, ClO, OCIO) and potential impacts on the atmosphere in the vicinity of volcanic plumes. In particular, we use MAX-DOAS data to study the formation of BrO and OCIO in the young plume in great detail and to infer typical formation times of these species (for the conditions at Mt. Etna in September 2012). We furthermore estimate mean plume abundances of BrO, ClO and OCIO. These results are used to derive Cl-atom concentrations in the plume in order to address the question of a potential – chlorine-induced – depletion of atmospheric methane ( $\text{CH}_4$ ) in the plume environment.

### 3 Methods and study area

#### 3.1 Technical setup

The MAX-DOAS instrument used in this study analyses the solar spectrum in the ultraviolet (UV) and the visible (VIS) ranges using two spectrographs (UV: Avantes AVA AvaBench-75-ULS2048x64; VIS: Avantes AVA AvaBench-75-ULS2048L) covering a spectral range of 292–578 nm (UV: 292.1–456.1 nm; VIS: 434.7–577.8 nm). Scattered sunlight was collected using a small telescope consisting of a quartz lens ( $f = 100$  mm) which focuses incoming light onto an optical fibre bundle. The latter consists of seven individual fibres each with a diameter of  $d = 100$   $\mu\text{m}$ . Six of these were coupled into the UV spectrograph, while the seventh fibre was connected to the VIS spectrograph. The measured spectral resolution of both spectrographs was  $\Delta\lambda_{\text{UV}} = 0.51$  nm and  $\Delta\lambda_{\text{VIS}} = 0.39$  nm. A *SCHOTT* BG-3 filter was placed behind the entrance slit of the UV spectrograph to reduce stray light. The telescope was focused such that both spectrographs have approximately the same field of view (UV:  $0.15^\circ$ , VIS:  $0.16^\circ$ , full aperture angle). The optical benches of the spectrographs were thermally insulated and temperature stabilised using a Peltier element controlled by a *Supercool* PR-59 temperature controller. During the whole measurement campaign, both spectrographs were stabilised to a temperature of  $T_{\text{meas}} = 10^\circ\text{C}$ . The air-tight instrument box was mounted onto a tripod. Two motors (azimuth and elevation) allowed to control the viewing direction of the tele-



**Figure 1.** Photo of the volcanic plume on 13 September, 07:24 UTC (09:24 LT), from the Etna observatory. It shows a slightly condensed plume as it could be observed in most cases during the campaign.

scope, geo-locations were recorded using a GPS receiver. All hardware elements were remotely controlled using an embedded PC. The software MS-DOAS was used for data acquisition. MS-DOAS was developed by U. Frieß at the Institute of Environmental Physics in Heidelberg and is designed to control standard hardware components used in DOAS instruments (e.g. spectrographs, motors, temperature controller, GPS receiver). Furthermore, it includes a scripting feature making it easily possible to automatise measurement and scanning routines.

#### 3.2 Measurement location and data acquisition

Mt. Etna is the largest and most active volcano in Europe and is situated in the eastern part of Sicily, an island south of the Italian mainland. The activity of Mt. Etna shows a distinct variability, including quiescent degassing periods as well as eruptive periods. During the measurement campaign in September 2012, Etna showed a stable quiescently degassing behaviour from the four active craters – north-east (NE), Bocca Nuova (BN), Voragine (VOR) and south-east (SE) crater – which are located in the summit region at an altitude of approximately 3300 m a.s.l. The first 3 days of the campaign (11–13 September 2012) took place at the Etna observatory (Pizzi Deneri) which is located approximately 2.5 km north-east of the active summit at an altitude of 2800 m. Figure 1 shows a photo of the volcano and the emission plumes from the different craters. The photo was taken from the observatory and shows the NE crater (right) and the SE crater (faint in the background) on 13 September at 07:24 UTC. The plume was slightly condensed (see Fig. 1) during most of the measurements performed in September 2012 and showed no visible indications of any ash emissions. In Fig. 2, all measurement locations of the campaign (11–26 September 2012) are indicated. One of the main objectives of this study was to investigate the temporal evolution of oxidised halogens in

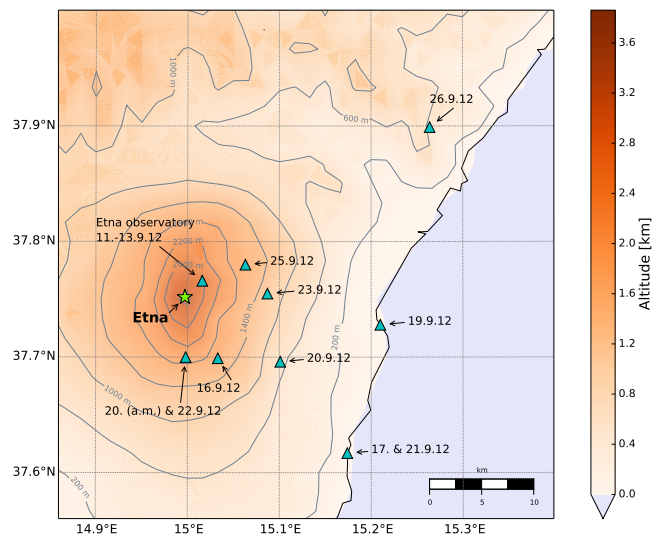


**Figure 2.** Measurement locations of the Etna campaign are indicated by blue triangles. The summit region with the four active craters (NE, BN, VOR and SE) is indicated by a green star.

the volcanic plume. Therefore, the measurements were performed at different locations in order to cover a large variety of different plume ages in the spectra.

### 3.3 Plume scanning routines

Three different plume scanning routines (“scans”) were performed in order to study the chemical variability of the measured species in the volcanic plume (see sketch in Fig. 3). One “scan” typically consists of a set of plume spectra plus a subsequently recorded solar reference spectrum with the telescope pointing into a volcanic gas free atmosphere (for details see Sect. 3.4).

#### 3.3.1 Plume evolution scans

The purpose of “plume evolution scans” is to study the chemical evolution of the measured species as a function of the plume age. The spectra are therefore recorded at different plume ages along the plume propagation direction (typically in the centre of the plume, see Fig. 3a).

#### 3.3.2 Plume cross-section scans

“Plume cross-section scans” are performed perpendicular to the plume propagation axis in order to study chemical variations between the centre and the edges of the plume (Fig. 3b).

#### 3.3.3 Point measurements

A certain number of spectra are taken at a fixed point in the plume without changing the viewing direction of the telescope. This measurement type is suited for the analysis of temporal variations in the plume composition (Fig. 3c).

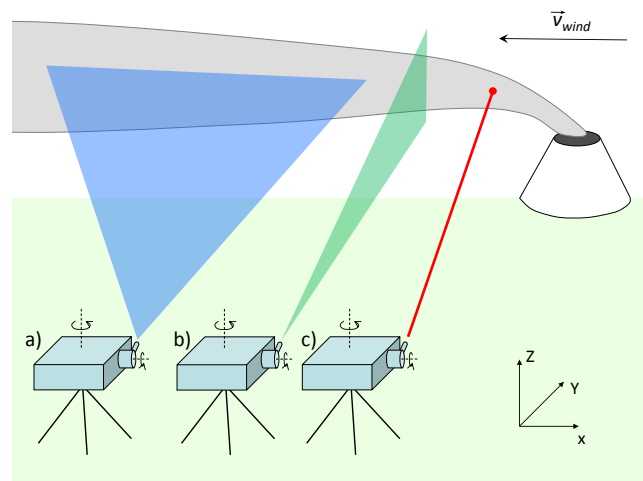


**Figure 3.** Sketch of the scanning routines: plume evolution scans (a, blue) scan stepwise along the plume propagation axis whereas plume cross-section scans (b, green) scan perpendicular to it. Point measurements (c, red) are performed at one spot in the plume without changing the telescope’s viewing direction.

### 3.4 Data acquisition and DOAS evaluation

The spectra were analysed using the software package DOASIS (v. 3.2.4422, Kraus, 2006). Details on the scanning routines can be found in Sect. 3.3. In order to improve the detection sensitivity, several hundred up to 1500 individual spectra were co-added for the DOAS analysis. A standard DOAS fit (see Platt and Stutz, 2008) was performed for the UV and VIS spectra in order to retrieve slant column densities (SCDs) of the chemical species in the plume (in this study mainly: OCIO, BrO, SO<sub>2</sub>, IO, OBrO, OIO). A Fraunhofer reference spectrum (FRS,  $I_0(\lambda)$ ) was included in the fitting routines to account for solar absorption lines in the spectra (Fraunhofer lines) and atmospheric background absorption. The FRS was recorded with the telescope pointing in the direction of a volcanic gas-free atmosphere and close in time to the corresponding plume spectra (usually subsequently to each scan). The latter is important to keep potential additional stratospheric signals at a minimum (for details see Sect. 3.9). Each potential FRS was pre-evaluated regarding its SO<sub>2</sub> content using a literature solar background spectrum as FRS (Chance and Kurucz, 2010) which was convolved with the instrumental line spread function (LSF). Only FRS candidates showing SO<sub>2</sub> SCDs ( $S_{\text{SO}_2}$ ) smaller than  $S_{\text{SO}_2, \text{FRS}} < 5 \times 10^{16}$  molecules cm<sup>-2</sup> were used as FRS.

In the following, the implemented steps to retrieve the SCDs from the raw spectra are described. Further details to individual topics regarding the data evaluation can be found in Appendix A.

Prior to the DOAS evaluation, all FRS and plume spectra were corrected for electronic offset and dark current. Two ring spectra ( $R$ ,  $R_4$ ) were included into the fitting routine

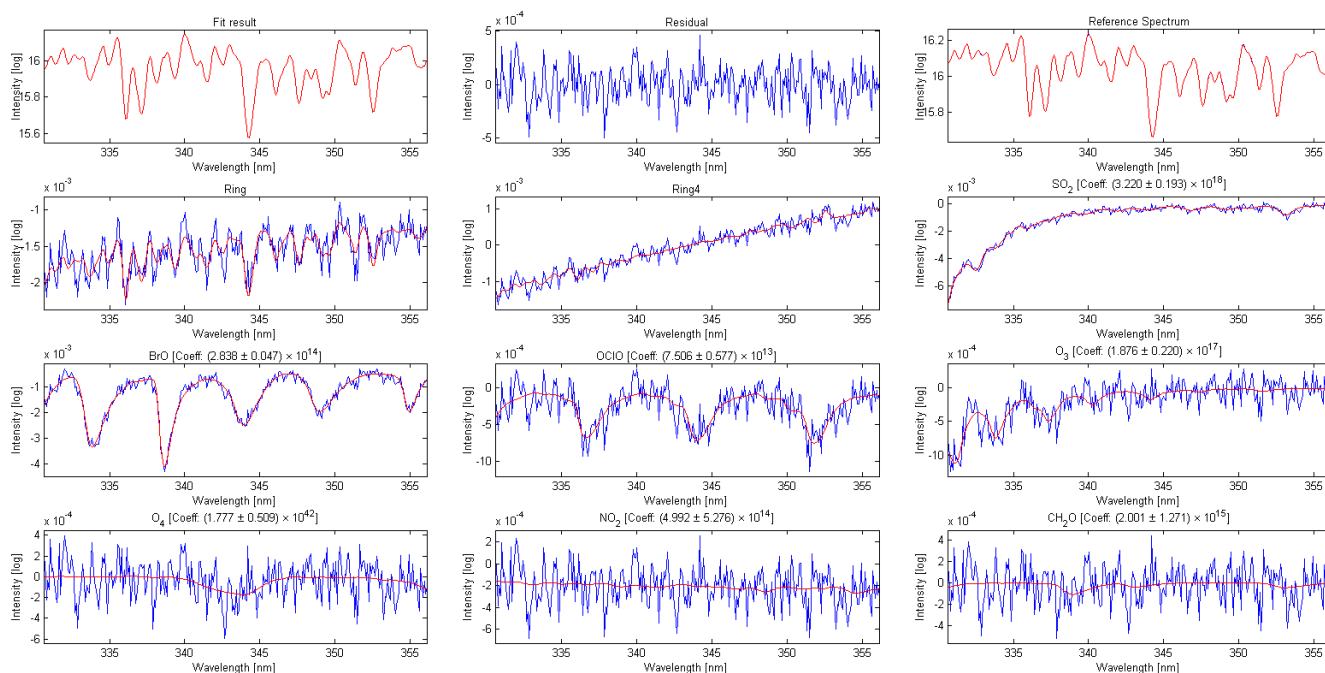


**Figure 4.** Exemplary fit result for the evaluation of BrO and OCIO in the wavelength range between 330.6 and 356.3 nm. This plume spectrum was recorded at the Etna observatory on 11 September 2012, 11:26 UTC; the corresponding FRS was recorded directly after the plume scan at 11:36 UTC. The BrO and OCIO-SCDs are  $S_{\text{BrO}} = 2.84 \times 10^{14}$  molecules  $\text{cm}^{-2}$  and  $S_{\text{OCIO}} = 7.51 \times 10^{13}$  molecules  $\text{cm}^{-2}$  respectively. In addition, the fit results of the two ring spectra ( $R$ ,  $R4$ ) and the additionally included absorbers ( $\text{SO}_2$ ,  $\text{O}_3$ ,  $\text{O}_4$ ,  $\text{NO}_2$ ,  $\text{CH}_2\text{O}$ ) are shown as well as the corresponding residual (peak-to-peak value:  $\overline{\Delta}_{\text{res}} = 9.65 \times 10^{-4}$ ).

to account for inelastic scattering effects (Raman scattering) in the atmosphere (see e.g. Vountas et al., 1998). The first ring spectrum ( $R$ ) was calculated in the usual way from the respective FRS using the function of the evaluation software DOASIS (Kraus, 2006). The second ring spectrum ( $R4$ ) was determined following the suggestions from Wagner et al. (2009) (for details see Appendix A1). Improvements due to the  $R4$  correction are discussed in Sect. A4, and a fit example with a strong  $R4$  signal is shown in Fig. A2. Literature cross sections of the individual absorbers ( $\sigma_i$ , see Table 2) were convolved with the LSF of the respective spectrograph. During the convolution, the  $\sigma_i$  were corrected for the solar  $I_0$  effect and for spectral saturation (Platt and Stutz, 2008) using the corresponding functions in DOASIS. The latter was performed assuming typical SCDs for the respective species (e.g.  $S_{\text{SO}_2} = 2 \times 10^{18}$  molecules  $\text{cm}^{-2}$ ). In order to correct for any misalignment of the spectrograph, a slight shift ( $\pm 0.1$  nm) and squeeze ( $\pm 5\%$ ) was allowed for all fitted species (i.e. FRS,  $R$ ,  $R4$ ,  $\sigma_i$ ). Shift and squeeze of all  $\sigma_i$  were linked to the strongest absorber and the two ring spectra were linked to the corresponding FRS in order to minimise the degrees of freedom during the fit-process. A third-order polynomial was included in the fitting routine to remove broad band extinction. An additional zero-order polynomial residing in intensity space was included (also referred to as offset polynomial) to account for intensity offsets in the spectra

(e.g. due to stray light, for details see Kraus, 2006; Platt and Stutz, 2008). The measurement uncertainty ( $\delta_{\text{meas}}$ ) was estimated conservatively by multiplying the retrieved fit errors ( $\delta_{\text{fit}}$ ) with a factor of  $U = 4$  to account for potential abundances of fit residuals structures (Stutz and Platt, 1996, see e.g. Fig. A2). In the case of good fit results (which were assessed by the peak-to-peak values of the fit residuals  $\overline{\Delta}_{\text{res}}$ ) the correction factor was reduced down to  $U = 3$  (i.e. for  $\overline{\Delta}_{\text{res}} \leq 1.2 \times 10^{-3}$ , see e.g. Fig. 4). Details regarding the error treatment are discussed in Sect. A2. The detection limits of the SCDs were defined to be twice the measurement uncertainty ( $2 \times \delta_{\text{meas}}$ ), thus representing a detection certainty of 95%.

### 3.5 Evaluation routines

The focus of this study was regarding the data collected with the UV spectrograph (i.e. the DOAS evaluation of OCIO, BrO,  $\text{SO}_2$ , IO). In order to find the optimum evaluation range for each species, detailed sensitivity studies were performed including DOAS fit contour plots (“retrieval wavelength mapping”, for details see Vogel et al., 2013). For the VIS data (i.e. the OBrO and OIO evaluation) these sensitivity studies were not performed since these data were of secondary interest. Therefore, we used a fixed correction factor of  $U = 5$  for the estimation of the corresponding measurement uncertainties of OBrO and OIO (for details see

**Table 1.** Evaluation routines of the different species and the corresponding wavelength ranges ( $\Delta\lambda$ ). Furthermore included are additional absorbers and the correction factors ( $U$ ) used to estimate the measurement uncertainty from the DOAS fit error. In the case of  $O_4$ , two different literature cross sections were used (labelled with (1) and (2), see also Table 2). The acronyms “uwr” and “lwr” indicate “upper” and “lower” evaluation wavelength ranges. Note: the two included ring spectra ( $R$ ,  $R4$ ) and the FRS are not included here (for details see Sect. 3.4).

Species	$\Delta\lambda$ [nm]	Additional absorbers	$U$
$SO_{2,lwr}$	314.8–326.8	$O_3$	3–4
$SO_{2,uwr}$	349.8–372.8	BrO, OCIO, $O_3$ , $O_4$ , $NO_2$ , $CH_2O$	3–4
BrO and OCIO	330.6–356.3	$SO_2$ , $O_3$ , $(1)O_4$ , $NO_2$ , $CH_2O$	3–4
OCIO <sub>uwr</sub>	363.6–391.3	$SO_2$ , $O_3$ , $(1)O_4$ , $NO_2$	3–4
IO	416.6–441.3	$H_2O$ , $NO_2$ , $(2)O_4$	3–4
OBrO	493.2–537.3	$H_2O$ , $NO_2$ , $O_3$ , $(2)O_4$	5
OIO	547.2–566.5	$H_2O$ , $NO_2$ , $O_3$ , $(2)O_4$ , OBrO	5

Sect. A2). All evaluation routines used in this study are summarised in Table 1, including the corresponding wavelength ranges, additional absorbers and the used correction factors  $U$  for the DOAS fit errors. An overview of all corresponding literature cross sections ( $\sigma_i$ ) used is given in Table 2. Note that in the case of  $O_4$ , two different literature cross sections were used because we found that different cross sections for the UV and VIS spectral ranges give the best results.

### 3.5.1 BrO and OCIO evaluation

BrO and OCIO were evaluated in the same wavelength range of  $\Delta\lambda_{BrO, OCIO} = 330.6\text{--}356.3$  nm. An exemplary fit result for this wavelength range is shown in Fig. 4, including the two ring spectra ( $R$ ,  $R4$ ) and all additionally included absorbers as well as the corresponding fit residual. This example shows a rather unstructured residual with a peak-to-peak value of  $\bar{\Delta}_{res} = 9.65 \times 10^{-4}$  (1200 co-added scans per spectrum); thus in this case a fit correction factor of  $U = 3$  was used.

Formaldehyde ( $CH_2O$ ) was included in the fitting routine in order to account for potential background abundances. In addition,  $CH_2O$  could also be formed in the volcanic plume itself, for instance via  $CH_4$  oxidation (in the plume most likely initiated by the reaction with Cl atoms) or in the presence of nitrogen oxides (Platt and Stutz, 2008).

OCIO was evaluated in a second “upper wavelength range” ( $\Delta\lambda_{OCIO,uwr} = 363.6\text{--}391.3$  nm) in order to verify the retrieved SCDs in the standard range with respect to possible influences due to radiative transfer phenomena and/or cross-correlations between different absorbers (for details see Appendix A3). However, this “upper” range was found to be influenced by larger fit uncertainties and was therefore not used

**Table 2.** Literature cross sections which were used in this study. Note that two different cross sections were used for  $O_4$ .

Trace gas	Literature cross section
$SO_2$	Hermans et al. (2009) (298 K)
BrO	Wilmouth et al. (1999) (298 K)
OBrO	Fleischmann et al. (2005) (298 K)
OCIO	Bogumil et al. (2003) (293 K)
$O_3$	Burrows et al. (1999) (221 K)
$(1)O_4$	Hermans et al. (2003)
$(2)O_4$	Greenblatt et al. (1990) (vacuum, modified by J. Burkholder)
IO	Spietz et al. (2005) (298 K)
OIO	Spietz et al. (2005) (298 K)
$NO_2$	Voigt et al. (2002) (293 K)
$H_2O$	Hitran database 2009 (273 K, 1020 hPa, 300–600 nm)
$CH_2O$	Meller and Moortgat (2000) (298 K)

for the discussion of our results. Nonetheless, both OCIO retrievals show a good correlation (see Fig. A1).

### 3.5.2 $SO_2$ evaluation

$SO_2$  was evaluated in two different wavelength ranges. The “lower wavelength range” (lwr) between  $\Delta\lambda_{SO_2,lwr} = 314.8$  and 326.8 nm (e.g. Vogel, 2011) was used for  $SO_2$  SCDs below  $3 \times 10^{18} \text{ cm}^{-2}$ . In this wavelength region, especially below 320 nm,  $SO_2$  shows strong absorption features. In order to avoid the well-known evaluation problems related to strong  $SO_2$  absorption in this “lower” wavelength range (see e.g. Kern et al., 2010; Bobrowski et al., 2010),  $SO_2$  was evaluated in a second, “upper” wavelength range of  $\Delta\lambda_{SO_2,uwr} = 349.8\text{--}372.8$  nm for  $SO_2$  SCDs exceeding  $3 \times 10^{18} \text{ cm}^{-2}$  (Hörmann et al., 2013). These problems – originating in the non-linear nature of the Beer–Lambert law – lead to an underestimation of the  $SO_2$  SCDs in the “lower” wavelength range. This is clearly visible in the scatter plot of the  $SO_2$  retrieval in both evaluation ranges shown in Fig. A3 (i.e. flattening of the trend at large  $SO_2$  SCDs). Furthermore, an exemplary fit result of the upper wavelength range is shown in Fig. A2).

### 3.5.3 IO, OIO and OBrO evaluation

In addition to the evaluation of BrO, OCIO and  $SO_2$ , abundances of IO, OBrO and OIO were investigated. The details of the corresponding evaluation routines for these species can be found in Table 1.

## 3.6 Estimation of OCIO and BrO concentrations from plume cross-section scans

The data from plume cross-section scans were used to estimate mean concentrations ( $\bar{c}_i$ ) of BrO and OCIO in the

plume. This was done assuming a circular plume cross section and straight line absorption light paths through the plume. Any potential deviations due to radiative transfer effects (RTE, e.g. multiple scattering, light dilution; for details see e.g. Kern et al., 2010; Mori et al., 2006) or deviations from the assumed circular shape were not considered in this estimation. The plume diameter ( $\varnothing_{\text{pl}}$ ) was estimated from the angular extend of the  $\text{SO}_2$  SCD profile and the distance to the plume (see also e.g. Bobrowski et al., 2003; Lee et al., 2005). The corresponding  $\text{SO}_2$  SCDs were used as a proxy for the lengths of the absorption light paths ( $l_{\text{eff},i}$ ) in the plume, whereas the largest  $\text{SO}_2$  SCD of the scan was assigned to  $\varnothing_{\text{pl}}$ . Based on that, the  $l_{\text{eff},i}$  could be estimated for all scan spectra  $i$ :  $l_{\text{eff},i} = \varnothing_{\text{pl}} / S_{\text{SO}_2, \text{max}} \times S_{\text{SO}_2, i}$ . Using this, the mean concentrations ( $\bar{c}_{j,i}$ ) of the measured species  $j$  (e.g. OCIO, BrO) were estimated:  $\bar{c}_{j,i} = S_{j,i} / l_{\text{eff},i}$ . The corresponding uncertainties were determined from the DOAS-fit errors and the uncertainties in the estimation of the plume diameter using Gaussian error propagation.

### 3.7 Determination of ClO concentrations

Following Kern et al. (2009), we estimated ClO concentrations from the retrieved BrO and OCIO-SCDs assuming steady state between the formation of OCIO (Reaction R7) and its photolytic destruction (Reaction R8):

$$\text{ClO} = \frac{J_{\text{OCIO}}}{k_7} \times \frac{[\text{OCIO}]}{[\text{BrO}]} \approx \frac{J_{\text{OCIO}}}{k_7} \times \frac{S_{\text{OCIO}}}{S_{\text{BrO}}}. \quad (1)$$

Since BrO and OCIO were evaluated in the same wavelength range, differences in the retrieved SCDs ( $S_i$ ) due to differences in the radiative transfer can be neglected. We therefore assume that the ratio of the OCIO and BrO concentrations is approximately the same as the ratio of the respective SCDs (Eq. 1). The OCIO photolysis frequencies  $J_{\text{OCIO}}$  used for the calculation of the ClO concentrations were simulated for our data set by E. Jäkel (Leipzig Institute for Meteorology). For the simulation, the 1-D radiative transfer model libRadtran (Mayer and Kylling, 2005) was used. The photolysis frequencies were determined for a set of chosen spectra from the field campaign and were between  $5.1 \times 10^{-2} \text{ s}^{-1}$  ( $\text{SZA} \approx 62^\circ$ ) and  $7.1 \times 10^{-2} \text{ s}^{-1}$  ( $\text{SZA} \approx 34^\circ$ ), slightly slower than typical values found in the stratosphere (e.g.  $J_{\text{str,OCIO}} \approx 7.6 \times 10^{-2} \text{ s}^{-1}$ ; Birks et al., 1977). Uncertainties in the determination of the ClO-concentrations were estimated using Gaussian error propagation.

### 3.8 Determination of the plume age ( $\tau$ ) and meteorological data

The plume age ( $\tau$ ) was estimated using meteorological information (i.e. wind speed and direction) and the measurement geometry (i.e. geo-locations of instrument and craters, telescopes viewing direction). A typical measurement geometry at Mt. Etna is sketched in Fig. 5. The intersection of the

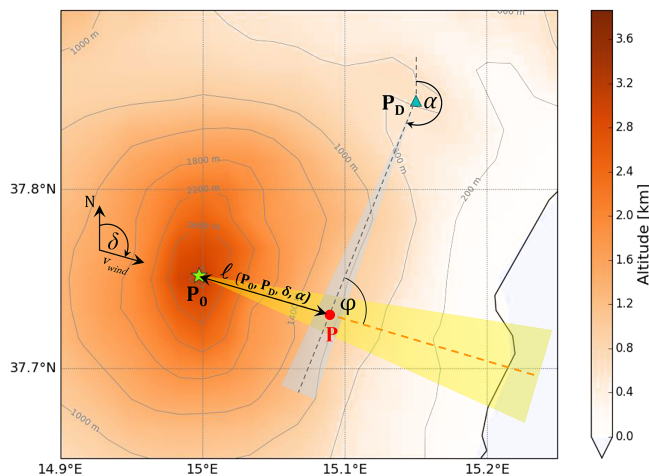


**Figure 5.** Typical scan geometry at Mt. Etna: the emission source is located at  $P_0$ , and the DOAS instrument is located at  $P_D$ . The intersection point of plume and telescope  $P$  is determined from the viewing direction of the telescope ( $\alpha$ , gray dotted line) and the plume direction ( $\delta$ , orange dotted line). Typical uncertainties of  $\alpha$  and  $\delta$  are indicated by the gray and yellow shaded area respectively. The plume age  $\tau$  is determined by dividing  $l(P_0, P_D, \delta, \alpha)$  by the wind velocity  $v_{\text{wind}}$ .

telescopes viewing direction with the plume determines the distance  $l$ . Based on that, the plume age was estimated as follows:

$$\tau = \frac{l}{v_{\text{wind}}}. \quad (2)$$

The azimuthal alignment of the instrument was performed using a compass. Due to possible disturbances of the planetary magnetic field by the volcano, we estimated the instruments azimuth-uncertainty to  $\pm 3^\circ$  (gray shaded area in Fig. 5). Wind directions were estimated using own observations/notes and – on clear days – satellite pictures from the MODIS network (Aqua, Terra satellites). Wind velocities were partly retrieved from simultaneously performed  $\text{SO}_2$ -camera measurements and from own observations. From the 16. September we additionally monitored meteorological data using a meteorological station, which was installed on the southern side of the craters. Uncertainties in the plume age estimation were determined using Gaussian error propagation, a detailed discussion of these, especially relative and absolute errors can be found in Appendix A5.

### 3.9 Correction for stratospheric BrO

Typical vertical column densities (VCDs) of stratospheric BrO are of the order of several  $10^{13} \text{ molecules cm}^{-2}$  (e.g. Schofield et al., 2004; Sinnhuber et al., 2005). Therefore, MAX-DOAS measurements of volcanic BrO (using scattered sunlight) can be significantly disturbed by stratospheric BrO signals under certain conditions. Based on the geo-

metrical air-mass factor (AMF:  $X = 1/\cos(\Theta)$ ) and by assuming a constant stratospheric BrO-VCD of  $V_{\text{str,BrO}} = 4.0 \times 10^{13}$  molecules  $\text{cm}^{-2}$  (Sinnhuber et al., 2005; Schofield et al., 2004) a correction was implemented to account for additional stratospheric BrO signals in our retrieved SCDs. A detailed discussion including simplifications and sensitivity studies can be found in Appendix A6.

For our data set, we found that deviations in the volcanic BrO column due to superimposed stratospheric BrO signals are smaller than 5% in 85% of the analysed spectra. Only 8% of the retrieved BrO SCDs showed deviations exceeding the corresponding fit uncertainty. All of these spectra were either recorded before 08:15 or after 16:45 LT ( $64.6^\circ < \text{SZA} < 83.2^\circ$ ), which shows the importance of this correction especially for measurements performed in the early morning and late afternoon.

### 3.10 SO<sub>2</sub> as volcanic plume proxy – analysis of $X_m O_n / \text{SO}_2$ ratios

In order to study spatial (and temporal) variations of the retrieved halogen species  $X_m O_n$ , molar SO<sub>2</sub> ratios of these species were analysed (i.e.  $X_m O_n / \text{SO}_2$  ratios), whereas SO<sub>2</sub> was treated as volcanic plume proxy due to its comparatively long tropospheric lifetime (e.g. McGonigle et al., 2004; Lee et al., 2011; Beirle et al., 2014). This is a common method to avoid signal variations due to atmospheric dilution effects (e.g. Bobrowski et al., 2003; Bobrowski and Platt, 2007; Bobrowski et al., 2007; Kern et al., 2009). Furthermore, compared to the individual SCDs the  $X_m O_n / \text{SO}_2$  ratios are much less affected by RTE such as light dilution or multiple scattering (Lübcke et al., 2014). We therefore neglect any potential influences of these effects on our retrieved trace gas ratios. The discussion of our results mostly relates to the measurements performed at the Etna observatory. Especially for these data, potential influences due to RTE on the retrieved ratios should be negligible because of the proximity to the plume, the relatively high altitude (i.e. low plume dilution; see e.g. Mori et al., 2006; Kern et al., 2010) and the fairly good visibility during most of the measurements (i.e. low aerosol scattering; for details see Sect. 3.2). The errors and detection limits of the  $X_m O_n / \text{SO}_2$  ratios were calculated from the SCD errors using Gaussian error propagation.

## 4 Results and discussion

Most of the significant OCIO detections (i.e. 99.2%) are related to the measurements performed at the Etna observatory (11–13 September 2012), where the largest SCDs can be found due to the proximity to the craters (little plume dispersion). Out of 677 significant SO<sub>2</sub> detections during the whole campaign, OCIO could be detected in 119 spectra up to plume ages of 6 min. BrO was detected in 452 spectra (269 of those recorded at the observatory) at plume ages up to

23 min. As expected, OCIO was less abundant compared to BrO with a mean OCIO / BrO ratio of 0.16. The retrieved SCDs of OCIO, BrO and SO<sub>2</sub> ranged between 0.4 and  $2.0 \times 10^{14}$  molecules  $\text{cm}^{-2}$ , 0.3 and  $11.4 \times 10^{14}$  molecules  $\text{cm}^{-2}$  and 0.03 and  $8.77 \times 10^{18}$  molecules  $\text{cm}^{-2}$  respectively. Furthermore, potential abundances of IO, OIO and OBrO were investigated but none of these species could be detected significantly. Upper limits of IO, OIO and OBrO were determined and are presented in Sect. 4.2.

### 4.1 OCIO and BrO results

In Fig. 6 we plotted all retrieved OCIO and BrO SCDs as a function of the corresponding SO<sub>2</sub> SCDs (A, B) and furthermore OCIO vs. BrO (C). Both BrO and OCIO show a good correlation to SO<sub>2</sub> (Fig. 6a, b), indicating that these species could only be detected in volcanic plume spectra. Average ratios of  $1.65 \times 10^{-4}$  for BrO/SO<sub>2</sub> (Fig. 6a) and  $3.17 \times 10^{-5}$  for OCIO/SO<sub>2</sub> (Fig. 6b) were found (linear regression). These values are in good agreement with previous findings (e.g. Bobrowski et al., 2007; Bobrowski and Giuffrida, 2012; General et al., 2015). For the linear regression, only significant detections at plume ages exceeding 3 min were considered (blue dots in Fig. 6). Measurements at plume ages smaller than 3 min (green dots) were excluded because in this plume age range the formation of BrO and OCIO is not yet fully developed and therefore the  $X_m O_n / \text{SO}_2$  ratios are smaller (for details see Sect. 4.1.3). The corresponding average OCIO/BrO ratio (at plume ages exceeding 3 min) is  $0.16 \pm 0.08$  and shows a very good correlation between both species in this plume age range ( $R^2 = 0.9447$ ). Young plume measurements (green dots,  $\tau < 3$  min), however, rather indicate stronger fluctuations of the OCIO/BrO ratio ( $R^2 = 0.4717$ ).

#### 4.1.1 Results from individual scans

In order to study the chemical evolution of BrO and OCIO, we analysed the corresponding ratios with SO<sub>2</sub> (BrO/SO<sub>2</sub>, OCIO/SO<sub>2</sub> ratio). In Fig. 7 examples of plume evolution scans of both ratios are plotted for different plume age ranges (i.e. Fig. 7a–e). Furthermore, an exemplary plume cross-section scan is shown in Fig. 7f. As discussed in Sect. 3.8 and Appendix A5, plume age errors were separated into a geometrical contribution ( $x$  error bars) and a percentage contribution due to uncertainties in the wind velocity ( $\Delta\tau$ , plot header). We explicitly point out again that these are not to be treated as independent random plume age errors between each of the scan spectra but are strongly correlated and, thus, indicate a stretch/squeeze of the whole data set towards smaller or larger plume ages. The plume evolution scans of the BrO/SO<sub>2</sub> ratio (Fig. 7a–c) show a strong increase in the young plume (Fig. 7a), stabilising after approximately 150 s downwind. This trend could be observed in six individual measurements performed in the young plume

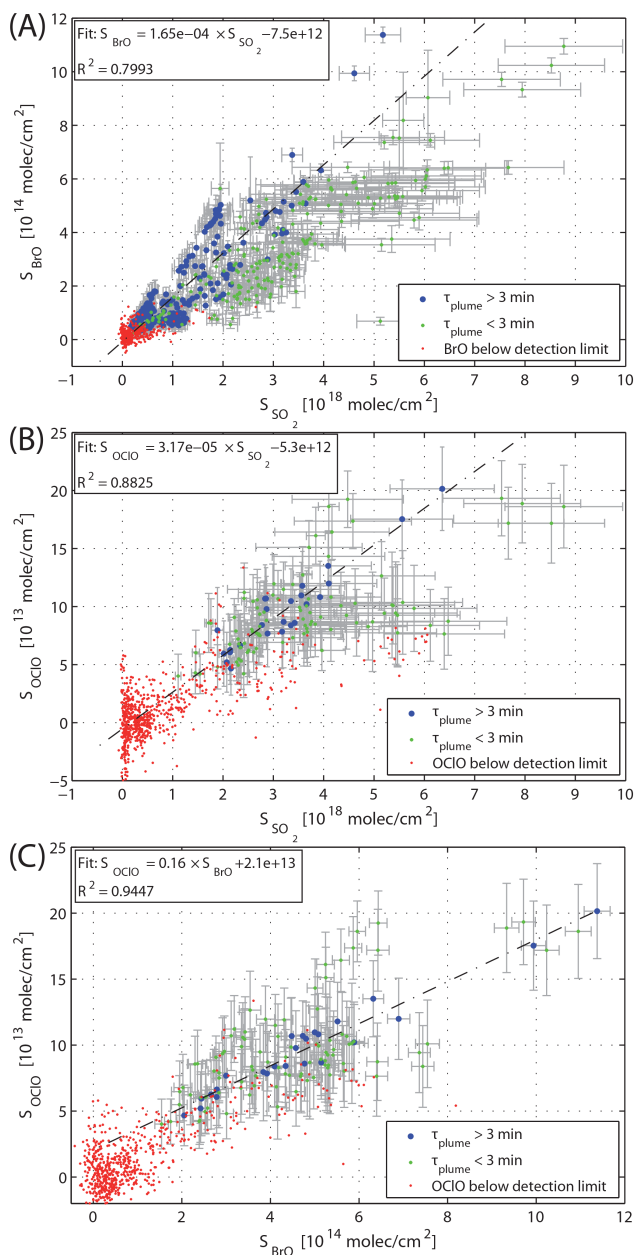


**Figure 6.** Retrieved slant column densities (SCDs) of BrO (a) and OCIO (b) as a function of the retrieved  $\text{SO}_2$  SCDs and (c), OCIO vs. BrO SCDs. The measurements were subdivided by their plume age  $\tau$  (i.e.  $\tau < 3$  min: green stars,  $\tau > 3$  min: blue dots) due to smaller BrO/ $\text{SO}_2$  and OCIO/ $\text{SO}_2$  ratios in the young plume (see also Sect. 4.1.3). Measurements below the detection limit of BrO (a) and OCIO (b) are indicated by red dots. We determined mean ratios in the  $\tau > 3$  min range (blue dots) by applying a linear fit and found values of BrO/ $\text{SO}_2 = 1.65 \times 10^{-4}$  and OCIO/ $\text{SO}_2 = 3.17 \times 10^{-5}$  respectively. The OCIO/BrO ratio (c) was found to be 0.16 for  $\tau > 3$  min and approximately 0.22 in the young plume.

(i.e.  $\tau < 5$  min); details are discussed in Sect. 4.1.3. At larger plume ages, the BrO/ $\text{SO}_2$  ratios show a rather constant behaviour with only slight variations. The discussion of potential trends of the corresponding OCIO/ $\text{SO}_2$  ratio in the young plume (at  $\tau \lesssim 2$  min) is more difficult for the results retrieved from the individual scans (see e.g. Fig. 7d–e), since the retrieved values are often below our (conservative) choice for the detection limit. Therefore, we refer to Sect. 4.1.3 where we statistically analyse and confirm these apparent trends of increasing BrO/ $\text{SO}_2$  and OCIO/ $\text{SO}_2$  ratios in the young plume. For plume ages exceeding 2 min, we found rather low variations in the retrieved OCIO/ $\text{SO}_2$  ratios (similar to our BrO observations for this plume age range, cf. Fig. 7e, b). Due to the higher  $S/N$  ratio, BrO could also be analysed at larger plume ages (i.e.  $\tau > 5$  min). An exemplary BrO scan in the aged plume is shown in Fig. 7c. It covers a plume age range between 8 and 22 min and shows rather stable BrO/ $\text{SO}_2$  ratios around  $1.7 \times 10^{-4}$ . A slight but not significant decrease of approximately 17 % might be observable between 8 and 10 min downwind.

The retrieved BrO/ $\text{SO}_2$  ratios in Fig. 7a–c range from  $8 \times 10^{-5}$  to  $1.8 \times 10^{-4}$  in the  $\tau > 3$  min regime (i.e. after reaching steady state). These variations could, for example, be caused by superimposed diurnal profiles (note: the scans were performed on different days and at different times) or varying volcanic activity.

#### 4.1.2 Cross-sectional distribution of BrO and OCIO

Previous studies showed increased BrO/ $\text{SO}_2$  ratios at the edges of the plume (e.g. Bobrowski et al., 2007; Louban et al., 2009; General et al., 2015). These are likely due to a limited transport of tropospheric  $\text{O}_3$  and  $\text{HO}_2$  radicals towards the plume centre (see also Sect. 2). Since OCIO is most likely formed in the “BrO+ClO” reaction, it is likely that also the OCIO/ $\text{SO}_2$  ratios show enhanced values at the edges of the plume. In order to elaborate this issue of increased  $X_m\text{O}_n/\text{SO}_2$  ratios at the edges of the plume, cross-section scans perpendicular to the plume propagation axis (see Fig. 3b) were performed. One exemplary plume cross-section scan of the BrO/ $\text{SO}_2$  ratio is shown in Fig. 7f. Please note the comparatively long time necessary to perform a full plume scan (here  $\sim 40$  min), which is due to the large number of co-added spectra in each measurement point. In order to investigate the issue of potentially increased ratios at the edges, we analysed the retrieved ratios of a given cross-section scan as a function of the corresponding  $\text{SO}_2$  SCDs (which indicate whether a spectrum was recorded in the centre or at the edge of the plume). In most of the scans, we found indications of increased ratios at the plume edges (i.e. at low  $\text{SO}_2$  SCDs compared to the corresponding “plume centre” spectra). However, from our data set these observations could unfortunately not be confirmed with certainty due to comparatively large measurement uncertainties at the plume edges (i.e. at small SCDs). This can be seen in the ex-

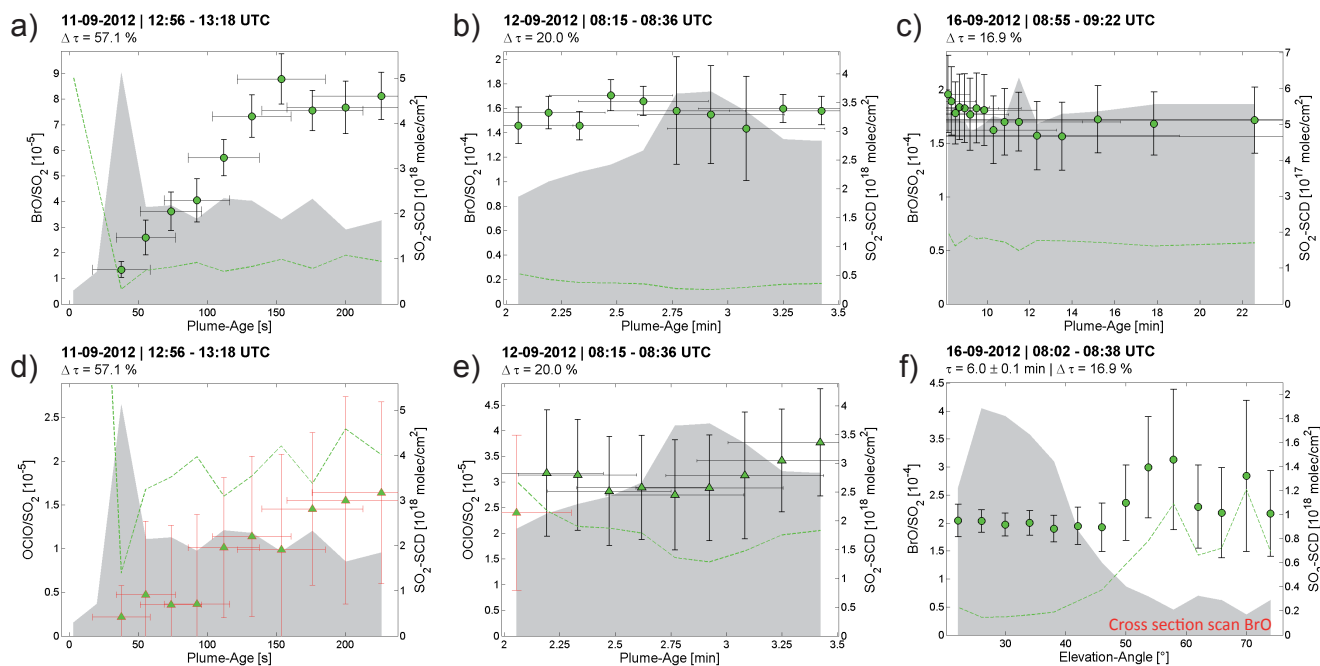


**Figure 7.** Plume evolution scans of the BrO/SO<sub>2</sub> ratio (a–c) and the OCIO/SO<sub>2</sub> ratio (d–e) (note the different time scales). A sample plume cross-section scan of BrO/SO<sub>2</sub> is shown in (f). The BrO/SO<sub>2</sub> (green circles) and the OCIO/SO<sub>2</sub> (green triangles) ratios are plotted with their corresponding detection limits (green dotted line). Red error bars indicate measurements below the detection limit. The SO<sub>2</sub> SCDs are plotted as gray shaded areas (right axis). The BrO/SO<sub>2</sub> ratio increases in the young plume and levels off at larger plume ages ( $\tau \lesssim 3$  min, a, b). The corresponding OCIO/SO<sub>2</sub> ratios (d, e) show a similar trend but are technically below the detection limit in the young plume (d). In (c), a plume evolution scan of the BrO/SO<sub>2</sub> ratio in the aged plume (8–22 min downwind) is shown. A rather stable trend is observable with indications of a slight decrease between 8 and 10 min downwind. In (f), a cross-section scan of BrO is plotted, showing indications of enhanced BrO/SO<sub>2</sub> ratios at low SO<sub>2</sub> SCDs (i.e. at the edges of the plume).

emplary cross-section scan shown in Fig. 7f, which also visualises the problems related to the plume edge spectra: the BrO/SO<sub>2</sub> ratios show increased values at low SO<sub>2</sub> SCDs, but considering the larger errors (due to low BrO and SO<sub>2</sub>-SCDs) it is not possible to draw any conclusions with certainty. However, by ignoring the comparatively large errors in the edge measurements and only analysing the absolute values of the retrieved ratios, we could observe this trend of increased BrO/SO<sub>2</sub> ratios at the edges in 76 % of all 25 suited cross-section scans. In the case of OCIO/SO<sub>2</sub> it was even more difficult to draw confident conclusions due to the weaker OCIO signal. Nonetheless, in five of – in total – nine suited cross-section scans, indications of enhanced OCIO/SO<sub>2</sub> ratios at low SO<sub>2</sub> SCDs could be found.

#### 4.1.3 The BrO and OCIO evolution in the plume

##### Statistical analysis of the young plume evolution

All plume evolution scans performed in the young plume clearly showed increasing BrO/SO<sub>2</sub> ratios at plume ages ( $\tau$ ) smaller than 150 s (see e.g. Fig. 7a). In the case of OCIO, we found strong indications of a similar trend in the young plume. However, from our individual scans this could not

be validated with certainty due to comparatively large measurement uncertainties in the OCIO retrieval (i.e. in most cases the OCIO/SO<sub>2</sub> ratios appeared to be below the detection limit in this plume age range, see e.g. Fig. 7d). In order to further elaborate this issue and especially the young plume evolution of OCIO, we therefore performed a statistical analysis of the retrieved  $X_m O_n / SO_2$  ratios as a function of the plume age. The plume was subdivided into six plume age intervals between 0 and 250 s downwind (i.e.  $\sim 42$  s interval<sup>-1</sup>) and the retrieved  $X_m O_n / SO_2$  ratios were assigned to the corresponding plume age interval accordingly. Only spectra related to the plume centre were considered by including only measurements showing SO<sub>2</sub> SCDs larger than  $1.5 \times 10^{18}$  molecules cm<sup>-2</sup>. This was done to avoid possible falsifications due to potentially enlarged ratios at the edges of the plume (for details see Sect. 4.1.2). Furthermore, we did not distinguish between measurements above or below the respective detection limits of BrO and OCIO. Based on this selection, we determined the mean value of the retrieved  $X_m O_n / SO_2$  ratios for each  $\tau$  interval. The corresponding uncertainties ( $\Delta$ , i.e. y axis error bars in Fig. 8) for the averaged ratios were determined from the mean of the individual errors ( $\bar{\sigma}_i$ ) divided by the inverse square root of the number  $N$  of averaged spectra in each interval:  $\Delta = \bar{\sigma}_i / \sqrt{N}$ .

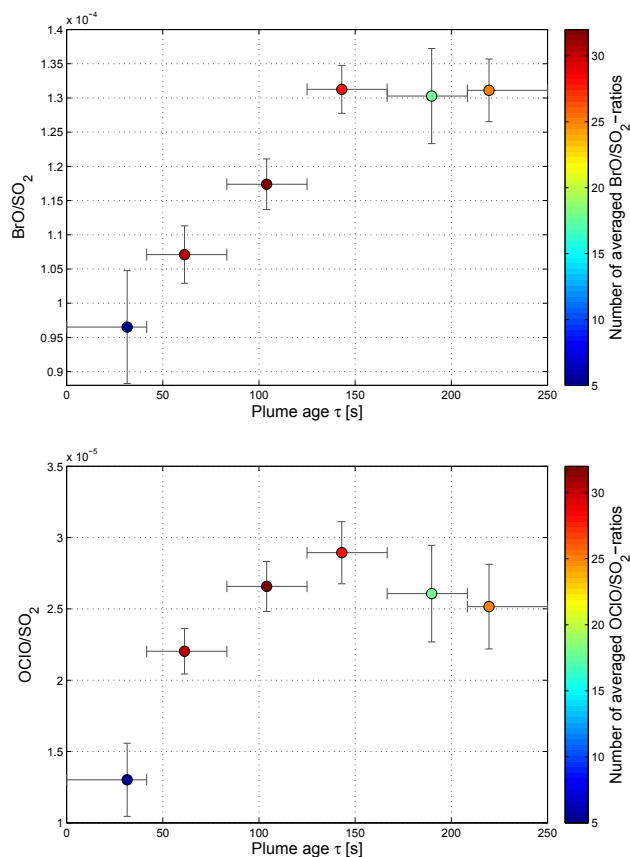


**Figure 8.** The young plume evolution of the BrO/SO<sub>2</sub> ratio (top) and the OCIO/SO<sub>2</sub> ratio (bottom): the colour code indicates the number of averaged individual measurements. The errors of the ratios were determined from the uncertainties of the individual measurements using Gaussian error propagation (for details see text). The horizontal error bars denote the respective plume age interval, which was used for averaging. The position of the averaged ratios for each plume age interval represents the mean plume age of the individual spectra included in this range. For both species, we observed an increase in the young plume levelling off at  $\tau = 142$  s. For larger plume ages, the BrO/SO<sub>2</sub> ratio shows rather constant values (at  $\sim 1.3 \times 10^{-4}$ ) whereas the OCIO/SO<sub>2</sub> ratio slightly decreases, which is probably due to plume dilution.

The results of this statistical approach are plotted in Fig. 8 and clearly show an increase of the OCIO/SO<sub>2</sub> ratio in the young plume. Furthermore, they confirm the increase of the BrO/SO<sub>2</sub> ratio which was already observed in the individual scans. Both BrO/SO<sub>2</sub> and OCIO/SO<sub>2</sub> level off after approximately 142 s. However, while BrO/SO<sub>2</sub> reaches a constant plateau of  $\sim 1.3 \times 10^{-4}$  at larger plume ages, the OCIO/SO<sub>2</sub> ratio rather seems to follow a slight – but statistically not significant – decreasing trend. Indications of such a decrease could also be observed in some of the individual scans and are likely due to plume dilution (decreasing BrO and ClO concentrations).

The retrieved BrO/SO<sub>2</sub> and OCIO/SO<sub>2</sub> ratios in the aged plume (i.e.  $\tau > 142$  s, see Fig. 8) are slightly lower compared to the values retrieved in the corresponding scatter plots (Fig. 6) of the whole data set (i.e.  $\overline{\text{BrO/SO}_2} = 1.65 \times 10^{-4}$ ,  $\overline{\text{OCIO/SO}_2} = 3.17 \times 10^{-5}$ ). One explanation for this deviation could be that spectra related to the plume edges (which showed indications of elevated BrO/SO<sub>2</sub> and OCIO/SO<sub>2</sub> ratios; see Sect. 4.1.2) were excluded in the statistical approach. Further possible reasons could be that the long-term trend of both species (i.e.  $\tau > 250$  s) is still increasing (which should, however, be unlikely for OCIO due to plume dilution) or that a superimposed diurnal signal might have influenced the statistics. Moreover, both long- and short-term variations of the volcanic activity might have affected the retrieved ratios. Nonetheless, the main objective of this study, namely the young plume increase of both species, could be validated. In order to further elaborate the long-term trend of BrO and OCIO (and/or diurnal profiles, variations due to volcanic activity), more measurements are necessary especially in the ageing plume.

The similarities in the trends of OCIO and BrO in the young plume (i.e. increase in the young plume and steady state after about 2–3 min) strongly support the assumption that OCIO is mainly formed via the “BrO + ClO” Reaction (R7).

#### 4.1.4 Photochemical formation of BrO and OCIO at low solar radiances

The “bromine explosion” includes the photolysis of the Br<sub>2</sub> molecule (Reaction R5, for details see Sect. 1). Kern et al. (2009) investigated night-time abundances of BrO at Masaya volcano, Nicaragua; however, they were not able to detect significant BrO levels during night-time.

Although MAX-DOAS measurements can only be made when a sufficient amount of sunlight is available, we were able to observe the onset of the BrO and OCIO formation. The corresponding point measurement (for details see Sect. 3.3) was performed in the early morning on 13 September 2012 between 05:20 and 06:20 UTC (SZA range: 83.2–70.1°, sunrise: 04:40 UTC). The data are plotted in Fig. 9 and clearly shows an increase of the BrO/SO<sub>2</sub> ratio with time between 05:20 and 05:32 UTC (see Fig. 9, top) and a constant ratio afterwards. A similar trend can be observed for the corresponding OCIO/SO<sub>2</sub> ratios (see Fig. 9, bottom) which were averaged (nearest-neighbour averaging) due to larger measurement uncertainties. Compared to BrO/SO<sub>2</sub>, the increase of OCIO/SO<sub>2</sub> appears to be delayed by approximately 30–40 min reaching a plateau around 06:15 UTC. One possible explanation for such a delayed increase could be that the availability of Cl atoms is delayed with respect to Br during this time of the day. The corresponding SO<sub>2</sub> profile is fairly constant showing typical plume centre values around  $5 \times 10^{18}$  molecules cm<sup>-2</sup>. This suggests that the measurement conditions (e.g. wind

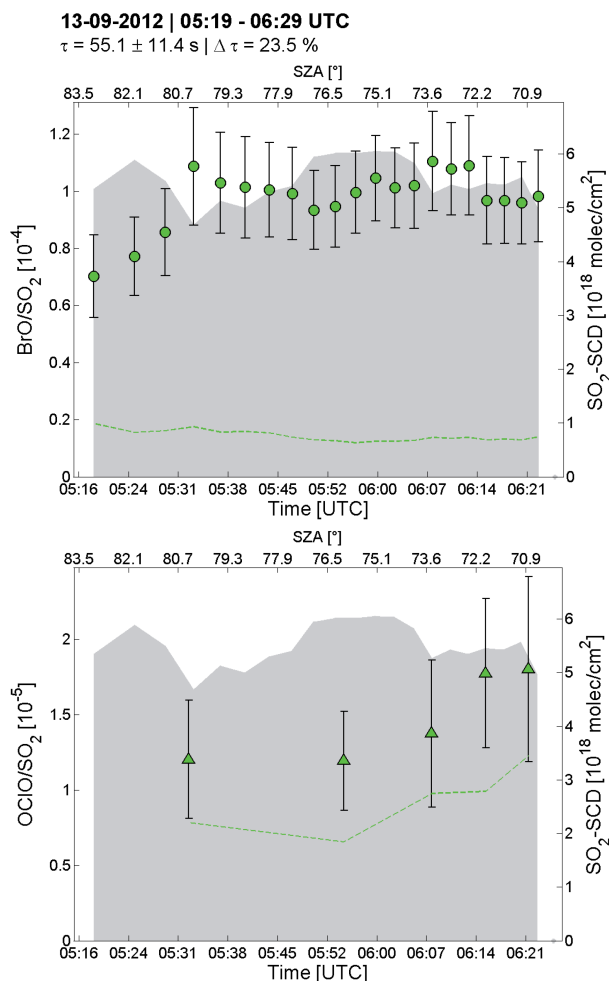


**Figure 9.** Early morning point measurement of BrO and OCIO: the BrO/SO<sub>2</sub> ratio increases between 05:17 and 05:32 UTC (top), reaching a plateau afterwards. The corresponding OCIO/SO<sub>2</sub> ratio also shows an increase which is delayed by approximately 30–40 min with respect to BrO (note that the OCIO/SO<sub>2</sub> ratios of this scan were averaged to increase the detection sensitivity; see also Sect. 4.1.3).

direction and velocity) did not change significantly during the measurement which is important for the interpretation of these data. In the case of BrO, this increase (at large SZAs) was only observable due to the correction for stratospheric BrO signals, where we assumed a constant stratospheric BrO VCD of  $V_{\text{str,BrO}} = 4.0 \times 10^{13}$  molecules cm<sup>-2</sup> (see Sect. 3.9). However, according to Schofield et al. (2004), slight variations of about 10–20% in the stratospheric BrO load are to be expected during that time of day (i.e.  $83.2^\circ > \text{SZA} > 80.3^\circ$ ). Hence, to ensure that the observed increase can be attributed to variations in the volcanic column (rather than stratospheric variations) we performed a sensitivity study for this data set by linearly varying the stratospheric VCD from 3.0 to  $4.0 \times 10^{13}$  molecules cm<sup>-2</sup> during the time span of the first five data points. This test did

not reveal any significant change and still clearly showed the increasing trend of the BrO/SO<sub>2</sub> ratio before 05:32 UTC. This is mainly due to the comparatively strong volcanic BrO signal of several  $10^{14}$  molecules cm<sup>-2</sup> during this measurement. We attribute this observation to be a direct result of the increasing solar irradiance at that time of the day (i.e. the increasing photolysis of Br<sub>2</sub> and BrCl molecules). This is further evidence that the availability of sunlight is an important parameter for the chemical processes related to the BrO and OCIO formation in volcanic plumes. On 22 September 2012, a similar point measurement was performed slightly later in the morning between 06:33 and 06:48 UTC (at  $\tau = 7.6 \pm 1.6$  min). It showed a constant BrO/SO<sub>2</sub> ratio of  $(1.15 \pm 0.2) \times 10^{-4}$  (20 spectra) which is in good agreement with the values shown in Fig. 9 after reaching the steady state. OCIO could not be detected in this scan.

#### 4.1.5 BrO, OCIO and ClO mixing ratios

As described in Sect. 3.6, average BrO and OCIO concentrations (volume number densities) were estimated from plume cross-section scans assuming a circular plume shape. The plume diameter could be estimated in 61 from a total of 90 cross-section scans performed during the campaign. Furthermore, ClO concentrations were calculated as described in Sect. 3.7. The corresponding number densities were converted into mixing ratios and the results are plotted in Fig. 10 as a function of the plume age  $\tau$ . Only BrO, ClO and OCIO concentrations above the detection limit were considered. Furthermore, only measurements during clear meteorological conditions were included to avoid potential impacts on the radiation light path, for instance caused by clouds or high background aerosol concentrations.

BrO mixing ratios between  $11(\pm 7)$  ppt and  $2.7(\pm 1.2)$  ppb were derived covering plume ages up to 17 min. The largest values were found in the young plume following a decreasing trend due to plume dilution. The OCIO mixing ratios ranged between  $37(\pm 24)$  and  $597(\pm 440)$  ppt and the corresponding values for ClO between  $70(\pm 44)$  and  $235(\pm 121)$  ppt. Both species could be detected up to 6 min downwind. Mean abundances in the young plume (i.e.  $\tau < 4$  min) were  $\overline{\text{ClO}} = 139 \pm 39$  ppt,  $\overline{\text{BrO}} = 1.35 \pm 0.45$  ppb and  $\overline{\text{OCIO}} = 300 \pm 90$  ppt.

The comparatively large errors of the derived mixing ratios (see Fig. 10) are due to our conservative estimation of the SCD errors and the uncertainties in the plume diameter estimation. More detailed radiative transfer effects (e.g. multiple scattering, light dilution; for details see Kern et al., 2010; Kern et al., 2012) were neglected in the determination of the mixing ratios as well as potential deviations from the circular plume cross section. Hence, the reported numbers are rather an estimate of the order of magnitude of the average plume abundances of these species. Nonetheless, for the ob-

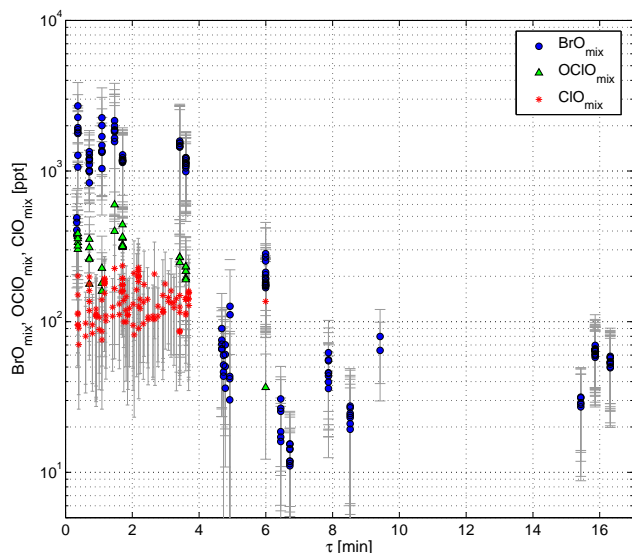


**Figure 10.** Mixing ratios of ClO, BrO and OCIO as a function of the plume age  $\tau$ . BrO and OCIO mixing ratios were determined directly from the retrieved SCDs assuming a circular plume cross section. ClO mixing ratios were determined from the BrO and OCIO SCDs assuming chemical equilibrium between the formation and destruction of OCIO. y-axis error bars were derived using Gaussian error propagation of the DOAS fit errors and the uncertainties in the estimation of the plume diameter (BrO and OCIO). Values between 70 and 235 ( $\pm 44$ –121) ppt (ClO), 11 and 2700 ( $\pm 7$ –1200) ppt (BrO) and 37 and 597 ( $\pm 24$ –440) ppt (OCIO) were found covering plume ages between 0 and 17 min. Mean abundances in the young plume (i.e.  $\tau < 4$  min) were ClO = 139 ppt, BrO = 1.35 ppb and OCIO = 300 ppt. Due to plume dispersion, the concentrations decrease with increasing plume age.

servatory data (11–13 September 2012, i.e.  $\tau < 4$  min range in Fig. 10) potential deviations due to RTE are most likely smaller than a factor of 2, relying on the findings of Kern et al. (2012) and Mori et al. (2006). This is due to the fairly good measurement conditions (i.e. low plume condensation, see e.g. Fig. 1) and furthermore because of the proximity to the plume (mean distance to plume:  $\bar{d} = 2.03$  km,  $d_{\max} < 3.2$  km) and the high altitude at the measurement location (i.e. 2800 m a.s.l., lower scattering probability). Moreover, a strong eccentricity of the plume (i.e. pronounced elliptical plume shape) is unlikely in this plume age regime (see e.g. Turner, 1970).

The measurements performed in the aged plume (i.e. data points at  $\tau > 4$  min in Fig. 10) are most likely stronger influenced by deviations from the assumed circular cross section and by the light dilution effect since they were partly performed at sea level and at greater plume distances (up to 17 km). Thus, the observed decrease of the BrO mixing ratios in the ageing plume (see Fig. 10) is most likely not solely due to the decreasing concentrations (plume dilution) but is probably also influenced by light dilution and elliptical plume

shapes. However, in most cases the latter two effects should counteract each other to a certain degree since light dilution induces a decrease in the “true” signal (i.e. the true signal is larger than the one derived from the measured SCDs), whereas for typical measurement geometries the lengths of the effective light paths ( $l_{\text{eff},i}$ ) through the plume are often underestimated (and thus the concentrations are overestimated). The latter is due to the pronounced elliptical shape of the plume (i.e.  $\sigma_{\text{hor}} > \sigma_{\text{vert}}$ , for typical conditions). At large plume viewing angles (i.e. close to the horizon)  $\sigma_{\text{vert}}$  is estimated from the scan (assuming  $\sigma_{\text{hor}} = \sigma_{\text{vert}}$  when using the method described in Sect. 3.6) and as a result the  $l_{\text{eff},i}$  are underestimated if the plume cross section is elliptical. A rough estimation assuming slightly stable conditions (i.e. Pasquill stability class E, see e.g. Turner, 1970) would approximately yield a factor of  $\sigma_{\text{vert}} / \sigma_{\text{hor}} \approx 0.16$  at 20 km distance from the source, yet the concentrations would be overestimated by up to a factor of 6 for the discussed measurement geometry (plume close to the horizon).

## 4.2 Results for IO, OIO and OBrO

We investigated the presence of IO (in the UV spectral range), OIO and OBrO (in the VIS spectral range) but did not detect any of these species. Here, we give both the detection limits for plume ages smaller and larger than 3 min (Table 3) since it appears reasonable to assume that these species – if abundant in the plume – show a similar plume evolution as was observed in the case of BrO and OCIO (for details see Sect. 4.1.3). For plume ages larger than 3 min, upper limits of  $5.2 \times 10^{-6}$  (IO / SO<sub>2</sub>),  $2.8 \times 10^{-5}$  (OIO / SO<sub>2</sub>) and  $1.8 \times 10^{-5}$  (OBrO / SO<sub>2</sub>) were found. Note that the UV spectrograph showed a better performance ( $S/N$  ratio) than the VIS spectrograph, which is indicated by the lower detection limits for IO compared to OIO and OBrO.

## 5 Conclusions

Simultaneous OCIO and BrO distributions were measured in the volcanic plume of Mt. Etna in September 2012 using the MAX-DOAS method. Measurements of volcanic OCIO are still rare and most reports are merely based on a few data points. Our results provide new, very detailed insights into the chemical evolution of these species in the volcanic plume. For the first time, the formation of both BrO and OCIO could be observed in a volcanic plume. These processes were studied in great detail and formation times of BrO and OCIO (i.e. the time until an equilibrium is reached) between 2 and 3 min downwind of the craters were found. Furthermore, mean concentrations of the order of several hundred ppt (ClO<sub>y</sub>, i.e. ClO, OCIO) up to several ppb (BrO) could be estimated. Keeping in mind that most of the ClO<sub>y</sub> and BrO<sub>y</sub> originates from the initially emitted HCl and HBr, our findings strongly suggest that the oxidation of chloride is much weaker com-

**Table 3.** Upper limits of IO, OIO and OBrO for the retrieved SCDs, the  $X_m O_n / SO_2$  ratios and the mixing ratios ( $r_i$ ). Note that the values do not correspond to the same plume spectrum but were determined individually.

Species	SCD [cm <sup>-2</sup> ]	$X_m O_n / SO_2$	$r_i$ [ppt]
Plume age $\tau < 3$ min			
IO	$8.6 \times 10^{12}$	$1.8 \times 10^{-6}$	29
OIO	$7.8 \times 10^{13}$	$2.0 \times 10^{-5}$	294
OBrO	$4.5 \times 10^{13}$	$1.1 \times 10^{-5}$	164
Plume age $\tau > 3$ min			
IO	$7.6 \times 10^{12}$	$5.2 \times 10^{-6}$	4
OIO	$7.5 \times 10^{13}$	$2.8 \times 10^{-5}$	25
OBrO	$3.6 \times 10^{13}$	$1.8 \times 10^{-5}$	12

pared to the bromide equivalent. This is mainly due to the fact that any potential Cl release mechanisms are likely less efficient compared to bromine. Moreover, once formed, the Cl radicals in the plume will rapidly react with CH<sub>4</sub>, which may even cause a significant depletion of CH<sub>4</sub> in the plume. This very important issue is addressed in the following, in which we use our results (i.e. the observed formation times of ClO<sub>y</sub>, see Sect. 4.1.3, and the estimation of mean concentrations, see Sect. 4.1.5) to derive an estimate of the Cl atom concentrations in the plume and, based on that, to investigate the potential of a chlorine-induced depletion of CH<sub>4</sub> in the plume environment.

### Cl-atom concentrations and the depletion of atmospheric CH<sub>4</sub> in the plume

Once Cl atoms are produced in a volcanic plume, they will rapidly react either with CH<sub>4</sub> or with O<sub>3</sub>:



The corresponding reaction rate coefficients are  $k_9 = 1.0 \times 10^{-13} \text{ cm}^3 \text{ s}^{-1}$  (Reaction R9 at 298 K) and  $k_{10} = 1.2 \times 10^{-11} \text{ cm}^3 \text{ s}^{-1}$  (Reaction R10 at 298 K; Sander et al., 2006). Note that Reaction (R9) is 16 times faster than the OH+CH<sub>4</sub> reaction (at 298 K) and has a strong positive temperature dependence (Sander et al., 2006). All other Cl sink reactions are much slower and are therefore neglected here.

Cl atom concentrations in the plume were estimated using the ClO and OCIO concentrations inferred from our measurements (see Sect. 4.1.5) and the corresponding young plume formation times  $\tau_0$  (see Sect. 4.1.3). For the estimation we assumed that the total amount of ClO<sub>y</sub> (i.e. [ClO<sub>y</sub>] = [ClO] + [OCIO]), observed after the levelling of OCIO (i.e. at plume age  $\tau_0$ ) was produced from Cl atoms via Reac-

**Table 4.** Retrieved Cl-atom concentrations (see Eq. 8) and the corresponding CH<sub>4</sub> lifetimes ( $\tau_{\text{CH}_4}$ ) according to Eq. (9). The values were determined for different background O<sub>3</sub> concentrations to account for potentially depleted O<sub>3</sub> in the plume.

Cl [cm <sup>-3</sup> ]	$\tau_{\text{CH}_4}$	O <sub>3</sub> [ppb]
$2.5 \times 10^6$	47 d	80
$5.0 \times 10^6$	23 d	40
$2.0 \times 10^7$	6 d	10
$2.0 \times 10^8$	14 h	1

tion (R10) (ClO) and Reaction (R7) (OCIO). Assuming a linear increase of [ClO<sub>y</sub>] the corresponding formation rate of Cl atoms was estimated as follows:

$$\left(\frac{d}{dt}[\text{Cl}]\right)_{\text{obs}} \approx \frac{d}{dt}[\text{ClO}_y] \approx \frac{[\text{ClO}_y](\tau = \tau_0)}{\tau_0}. \quad (3)$$

Actually the true rate of Cl atom production  $d/dt[\text{Cl}]$  is larger since a fraction of the Cl atoms reacts with CH<sub>4</sub> (Reaction R9) and never shows up as ClO<sub>y</sub> (possible reaction of Cl with other hydrocarbons is likely to be unimportant and was therefore neglected here):

$$\frac{d}{dt}[\text{Cl}] \approx \left(\frac{d}{dt}[\text{Cl}]\right)_{\text{obs}} \times \frac{1}{K} \quad (4)$$

with

$$K = \frac{[\text{O}_3] \times k_{10}}{[\text{O}_3] \times k_{10} + [\text{CH}_4] \times k_9}. \quad (5)$$

The corresponding Cl-atom concentration is then given by

$$[\text{Cl}] = \frac{d}{dt}[\text{Cl}] \times \tau_{\text{Cl}} \approx \frac{d}{dt}[\text{ClO}_y] \times \frac{1}{K} \times \tau_{\text{Cl}}, \quad (6)$$

whereas the lifetime of Cl ( $\tau_{\text{Cl}}$ ) was estimated by

$$\tau_{\text{Cl}} = \frac{1}{[\text{O}_3] \times k_{10} + [\text{CH}_4] \times k_9}. \quad (7)$$

Introducing the expression for  $\tau_{\text{Cl}}$  in Eq. (6) and using Eq. (3), an estimate of the Cl-atom concentration can be obtained:

$$[\text{Cl}] = \frac{\frac{d}{dt}[\text{ClO}_y]}{[\text{O}_3] \times k_{10}} \approx \frac{[\text{ClO}_y]}{\tau_0 \times [\text{O}_3] \times k_{10}}. \quad (8)$$

Based on this the CH<sub>4</sub> lifetime in the plume (due to reaction with Cl, see Reaction R9) can be derived:

$$\tau_{\text{CH}_4} \approx \frac{1}{[\text{Cl}] \times k_9} \approx \frac{\tau_0 \times [\text{O}_3] \times k_{10}}{[\text{ClO}_y] \times k_9}. \quad (9)$$

Note that  $\tau_0$  denotes the formation time of OCIO as introduced in Sect. 4.1.3, whereas  $\tau_{\text{CH}_4}$  corresponds to the methane lifetime in the plume.

For the estimation of  $\text{ClO}_y$ , we determined mean ClO and OCIO concentrations from our retrieval considering only plume ages between 120 and 240 s (see also Sect. 4.1.5). We retrieved values of  $\overline{\text{ClO}} = 2.0 \times 10^9 \text{ cm}^{-3}$  and  $\overline{\text{OCIO}} = 3.7 \times 10^9 \text{ cm}^{-3}$  respectively and hence  $\overline{\text{ClO}_y} = 5.7 \times 10^9 \text{ cm}^{-3}$ . Based on our findings discussed in Sect. 4.1.3 we estimated the  $\text{ClO}_y$  formation duration to be  $\tau_0 = 142 \text{ s}$ . The OCIO concentrations (used to estimate  $\text{ClO}_y$ ) might carry potential uncertainties due to RTE or non-circular plumes. However, as discussed in Sect. 4.1.5, these deviations should be small (i.e.  $\lesssim 2$ ) for the majority of data points recorded in the young plume and should therefore not significantly influence the outcome of this analysis. The typical tropospheric  $\text{O}_3$  background is 60–80 ppb for this (relatively polluted) region and altitude (Kalabokas et al., 2013). The expected  $\text{CH}_4$  lifetime in the plume is directly proportional to the prevailing  $\text{O}_3$  concentration (Eq. 9). Since  $\text{O}_3$  is most likely depleted in the plume (von Glasow, 2010; Kelly et al., 2013) we determined  $[\text{Cl}]$  and  $\tau_{\text{CH}_4}$  under variation of the  $\text{O}_3$  concentration (assuming  $\text{O}_3$  mixing ratios between 1 and 80 ppb). Our results are summarised in Table 4 and show relatively small Cl-atom concentrations (i.e.  $10^6$ – $10^8 \text{ cm}^{-3}$ ) and  $\text{CH}_4$  lifetimes between 14 h and up to 47 days. These lifetimes are more than 2 orders of magnitude shorter than the average atmospheric lifetime of  $\text{CH}_4$ .

However, if  $\text{O}_3$  is not strongly depleted,  $\text{CH}_4$  destruction by Cl atoms will probably not lead to a detectable loss of  $\text{CH}_4$  in the plume since the Cl levels derived from our measurements (at plume age  $\tau = 142 \text{ s}$ ) should decrease rapidly as the plume disperses. Even if these Cl levels would prevail for a few hours downwind, only a small fraction (less than 1 %) of the  $\text{CH}_4$  would be destroyed (assuming that the mean  $\text{O}_3$  levels in the plume exceed 10 ppb). However, in regions of very low  $\text{O}_3$  concentrations (i.e. possibly in the plume centre; von Glasow, 2010), a significant loss of  $\text{CH}_4$  could be present but the atmospheric impact would probably still be negligible since the effective volume of this potential methane-depleting environment would be very small. Nevertheless, we want to remark that our calculations are based on the volcanic conditions at Mt. Etna in September 2012, and we therefore want to stress that it is absolutely possible that  $\text{CH}_4$  depletion may become detectable in plumes of other volcanoes or at different conditions (e.g. due to varying volcanic activity, stronger chlorine emissions, larger  $\text{Cl}^-/\text{Br}^-$  ratios, low NMHC (non-methane hydrocarbons) concentrations or the presence of volcanic particles favouring the chloride oxidation).

## Appendix A: Details regarding the data evaluation

### A1 Details regarding the additional $R4$ spectrum

In addition to the standard ring spectrum (calculated using the software DOASIS; Kraus, 2006), a second ring spectrum ( $R4$ ) was determined as follows (for details see Wagner et al., 2009, Appendix B therein):

$$R4(j) = R(j) \times \left( \frac{\lambda(j)}{\lambda_0} \right)^4 - R(j). \quad (\text{A1})$$

Here,  $j$  denotes the pixel on the detector,  $\lambda(j)$  the appropriate wavelength and  $\lambda_0$  the central wavelength of the evaluation range.  $R(j)$  denotes the intensity of the ring spectrum at detector channel  $j$ . Note that the  $R4$  spectrum was orthonormalised with respect to  $\lambda_0$ .

The  $R4$  spectrum accounts for influences due to multiple scattering and/or scattering on aerosols and cloud particles which are not considered in the determination of  $R$ . Improvements due to the  $R4$  correction are discussed and visualised in Sect. A4 and in Fig. A2.

### A2 DOAS error treatment

According to Stutz and Platt (1996) the error of atmospheric trace gas measurements with the DOAS technique does not purely arise from pure photon (shot) noise and is thus not entirely statistical (Poisson statistics). The fit residuals often show distinct structures which are mainly a result of the limited optical resolution of the instrument or due to uncertainties in the absorption spectra of the fitted species. In this case, the DOAS fit yields underestimated measures of the true fit uncertainty since the fitting routine is based on the assumption of individual radiance measurements in each pixel on the detector. Thus, in the case of structured fit residuals, this underestimation has to be accounted for. This can be done by multiplying the retrieved DOAS fit errors with a certain factor (here denoted with  $U$ ) which can reach values of up to 6 according to Stutz and Platt (1996). The choice of  $U$  for a given measurement is mainly dependent on the spectral width of the fitted absorption lines and on the width of potentially abundant residual structures (measured in channels on the detector; see Fig. 10 in Stutz and Platt, 1996). Since we could observe such residual structures in some of our measurements (see e.g. Fig. A2), we followed Stutz and Platt (1996) and corrected our retrieved DOAS fit errors with a factor of  $U = 4$ . We remark that this constitutes a conservative estimation of the measurement uncertainty. Therefore, in the case of good fit results (i.e. low peak-to-peak value of the fit residual,  $\overline{\Delta_{\text{res}}}$ ), this factor was reduced as follows:

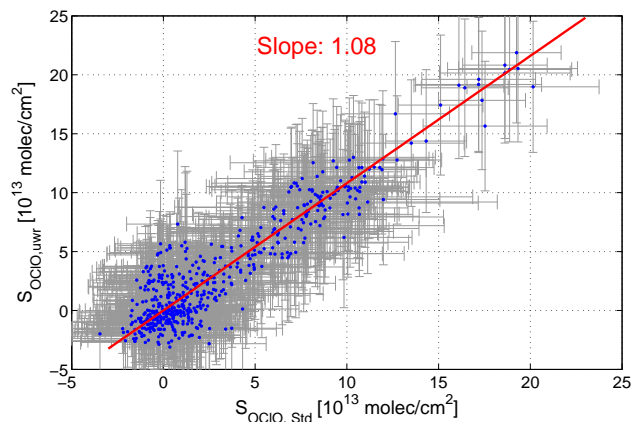


**Figure A1.** Retrieved OCIO SCDs from the standard (“Std”) evaluation range  $\text{OCIO}_{\text{Std}}$  (330.6–356.3 nm) and the second “upper” wavelength range for the evaluation of  $\text{OCIO}_{\text{uwr}}$  (363.6–391.3 nm). The values show good coincidence within their uncertainties with slightly larger SCDs ( $\sim 8\%$ ) in the upper wavelength range.

- (i)  $\overline{\Delta_{\text{res}}} > 1.5 \times 10^{-3}$   
 $\Rightarrow U = 4$  (see e.g. Fig. A2),
- (ii)  $1.5 \times 10^{-3} \geq \overline{\Delta_{\text{res}}} > 1.2 \times 10^{-3}$   
 $\Rightarrow U = 3.5$ ,
- (iii)  $1.2 \times 10^{-3} \geq \overline{\Delta_{\text{res}}}$   
 $\Rightarrow U = 3$  (see e.g. Fig. 4).

We found a good correlation between  $\overline{\Delta_{\text{res}}}$  and the width of structures in the residual. However, we want to point out that this approach constitutes only a rough – but easy to implement and still conservative – implementation of the interpretation of the retrieved DOAS fit errors (e.g. Donovan et al., 2014, used a fixed correction factor of  $U = 3$  for their OCIO and BrO evaluation). In Fig. A2 such an example of a structured residual is shown (one residual structure is marked and has a width of  $W \approx 20$ – $30$  channels on the detector). Typical absorption lines of the fitted species cover between 15 and 30 channels on the detector of our spectrograph. Considering these typical widths, we decided to use fit correction factors between 3 and 4, based on the findings of Stutz and Platt (1996) (see especially Fig. 10 therein).

### A3 Alternative OCIO evaluation routine ( $\text{OCIO}^{\text{uwr}}$ )

OCIO was additionally evaluated in a second range between 363.6 and 391.3 nm covering three OCIO absorption bands. Besides the two ring spectra and the FRS, reference spectra of  $\text{SO}_2$ ,  $\text{O}_3$ ,  $\text{O}_4$  and  $\text{NO}_2$  were additionally included. In principle, an advantage of this “upper” wavelength range should be that it is less influenced by potential cross correlations with BrO,  $\text{O}_3$  or  $\text{CH}_2\text{O}$  in the DOAS fit. However, it was

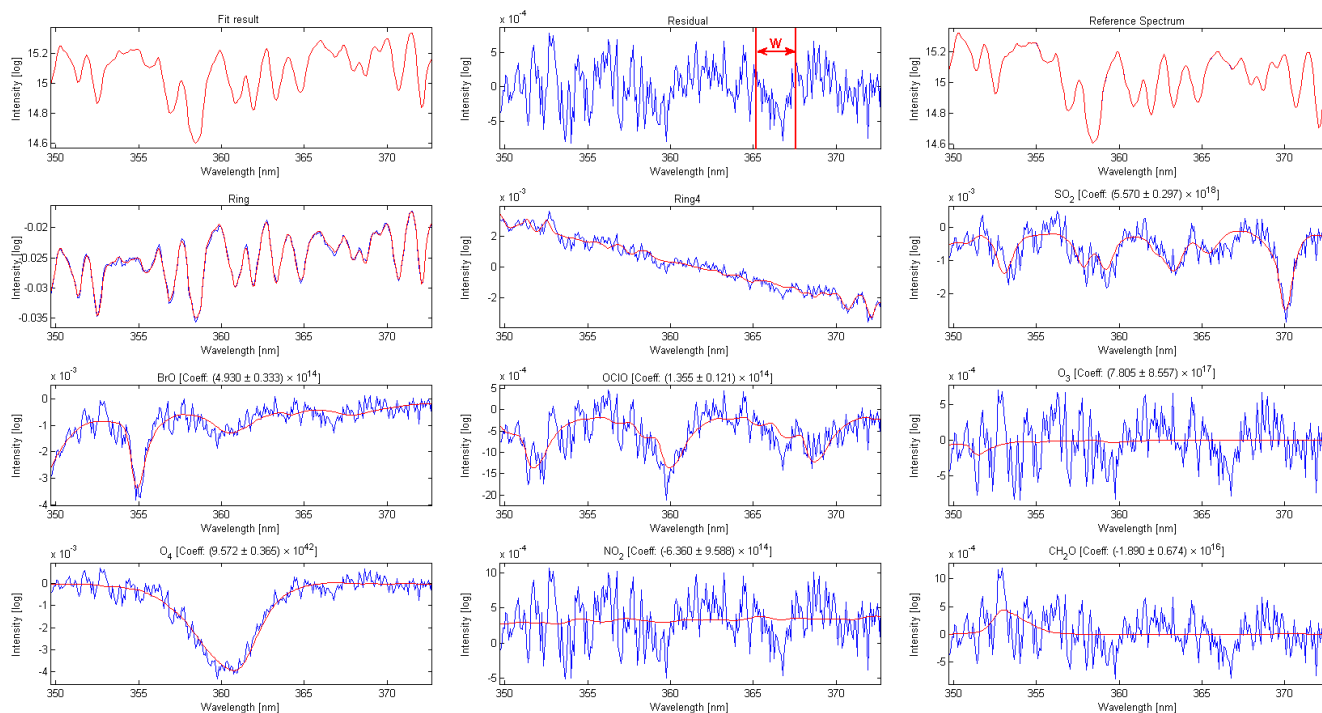


**Figure A2.** Exemplary fit result for the  $\text{SO}_2$  upper evaluation range between 349.8 and 372.8 nm. The corresponding plume spectrum was recorded at the Etna observatory on 13 September 2012, 06:20 UTC, showing a  $\text{SO}_2$  SCD of  $S_{\text{SO}_2} = 5.57 \times 10^{18}$  molecules  $\text{cm}^{-2}$ . In addition, the fit results of the two ring spectra ( $R$ ,  $R4$ ) and the additionally included absorbers ( $\text{SO}_2$ ,  $\text{O}_3$ ,  $\text{O}_4$ ,  $\text{NO}_2$ ,  $\text{H}_2\text{CO}$ ) are shown as well as the corresponding residual (peak-to-peak value:  $\Delta_{\text{RES}} = 1.60 \times 10^{-3}$ ,  $\chi^2 = 3.00 \times 10^{-5}$ ). In this example, the residual is rather structured and one typical structure was marked showing a width  $W$  between 20 and 30 channels on the detector. Please note that  $\text{CH}_2\text{O}$  was falsely detected in this fit (considering the fit error) due to the relatively structured residual. This shows the importance of the used fit correction factors  $U$ . Please also note the improvements due to the fitted  $R4$  spectrum, which are discussed in more detail in the text in Sect. A4.

found that the fits often showed distinct residual structures in this wavelength range, resulting in relatively large fit uncertainties compared to the standard evaluation range for OCIO (Sect. 3.5.1). These structures are most likely caused by distinct solar Fraunhofer lines present in this wavelength region which can cause a strong ring effect. Nevertheless, the retrieved OCIO SCDs show a good correlation with slightly larger SCDs ( $\approx 8\%$ ) in the upper wavelength range (see Fig. A1).

#### A4 Details regarding the $\text{SO}_2$ evaluation

$\text{SO}_2$  was evaluated in two wavelength ranges in order to account for radiative transfer effects due to strong absorption at large  $\text{SO}_2$  column amounts in the wavelength regime below 320 nm. An exemplary fit result of the  $\text{SO}_2$  evaluation in the alternative “upper”  $\text{SO}_2$  range ( $\Delta\lambda_{\text{SO}_2, \text{uwr}} = 349.8\text{--}372.8$  nm) is shown in Fig. A2 showing a comparatively large  $\text{SO}_2$  SCD of  $S_{\text{SO}_2, \text{uwr}} = 5.57 \times 10^{18}$  molecules  $\text{cm}^{-2}$ . The corresponding  $\text{SO}_2$  SCD in the lower evaluation range was found to be smaller (as expected) and amounts to  $S_{\text{SO}_2, \text{lwr}} = 4.89 \times 10^{18}$  molecules  $\text{cm}^{-2}$ . The corresponding plume spectrum was recorded during the early morning point measure-

ment discussed in Sect. 4.1.4 at 06:20 UTC on 13 September 2012. The FRS was recorded subsequently at 06:25 UTC, explaining the low  $\text{O}_3$  SCD. This example clearly shows the necessity of our conservative approach for the fit error estimation: in contrast to the BrO and OCIO fit example (given in Sect. 3.4, Fig. 4), this fit example shows a rather structured fit residual (most likely due to the strong ring effect in this spectrum). This even causes a “false” detection of  $\text{CH}_2\text{O}$  in this spectrum, showing a negative (but significant) SCD of  $S_{\text{CH}_2\text{O}} = -1.89 \pm 0.67 \times 10^{16}$  molecules  $\text{cm}^{-2}$  (i.e.  $\text{CH}_2\text{O}$  could not be detected in the standard evaluation range in this spectrum). Hence, using only the uncorrected DOAS fit error would yield a significant detection of  $\text{CH}_2\text{O}$  in this case (even within  $3\sigma$  confidence). This demonstrates the tremendous importance of applying appropriate fit correction factors to account for these effects (as discussed in Sect. A2). The example given in Fig. A2 also clearly shows the significance of the  $\lambda^{-4}$  dependency of the ring effect due to the relatively strong ring signal (i.e. ring optical densities of the order of  $10^{-2}$ ), accounted for by fitting the  $R4$  spectrum (Sect. A1). Here, the  $R4$  correction leads to a fit improvement of 25% in the  $\chi^2$  of fit residual ( $\chi^2$  is reduced from  $4.02 \times 10^{-5}$  to  $3.00 \times 10^{-5}$ ) and furthermore to a reduction

in the total residual amplitude (i.e. peak-to-peak value) by 33 % compared to the same fit excluding the R4 spectrum (i.e.  $\overline{\Delta}_{\text{res}} : 2.39 \times 10^{-3} \xrightarrow{R4} 1.60 \times 10^{-3}$ ).

Figure A3 shows a scatter plot of the retrieved SO<sub>2</sub> SCDs in both evaluation ranges. The retrieved values show good coincidence within their errors up to SO<sub>2</sub> SCDs around  $4 \times 10^{18}$  molecules cm<sup>-2</sup>. For larger SCDs the trend starts to flatten due to the underestimated SCDs in the lower evaluation range.

#### A5 Uncertainties and simplifications in the plume age determination

The main uncertainties related to the plume age determination using Eq. (2) are due to uncertainties in the wind velocity and the determination of  $l$  (i.e. mainly due to uncertainties in  $\delta$  and  $\alpha$ , see Fig. 5). We thus subdivided our error-representation of the plume age  $\tau$  into two contributions. The first (in the following denoted as  $\Delta\tau_l(\alpha, \delta)$ ) is determined from the uncertainties in  $\alpha$  and  $\delta$  (mainly geometrical uncertainties).  $\Delta\tau_l(\alpha, \delta)$  can vary strongly between different spectra from plume evolution scans due to the nature of the trigonometric functions involved in the calculation of  $l$ .  $\Delta\tau_l(\alpha, \delta)$  is therefore plotted for each spectrum separately in form of  $x$ -axis error bars (see e.g. Fig. 7). The second contribution (in the following denoted as  $\Delta\tau$ ) to the plume age error is caused by uncertainties in the wind velocity  $\Delta v_{\text{wind}}$  which have a linear effect on the plume age uncertainty ( $\partial\tau/\partial v_{\text{wind}} \propto \Delta v_{\text{wind}}$ ). Since  $\Delta\tau$  is independent of the measurement and plume angles, its relative impact on each spectrum ( $\Delta\tau/\tau$ ) is constant. The corresponding contribution is therefore given as a percentage value in the plot header (see e.g. Fig. 7).

For simplicity, we reduced the determination of  $\tau$  to a 2-D problem in the horizontal plane, because differences in the altitude between plume and DOAS instrument have only a small influence on the determination of  $\tau$  for typical scanning geometries (and a wind driven, horizontal plume propagation).

Furthermore, by reducing the volcanic plume and the telescopes viewing direction to a line (dotted lines in Fig. 5) we did not consider any effects caused by plume dispersion or the telescope's field of view for our estimation of  $\tau$ . These effects are usually negligible for typical scan geometries ( $\varphi \approx 90^\circ$ , see Fig. 5) and may need to be considered when the measurements are performed at small angles  $\varphi$ . In this case the analysed light has penetrated a multiple of different plume ages which essentially causes a smoothing of the signal with respect to  $\tau$ . The corresponding impact regarding the interpretation of the data both depends on the desired temporal resolution of the respective scan (i.e.  $\Delta\tau$  between individual scan spectra) and on the chemical variability of the analysed species in the analysed plume age range.

A further simplification in our algorithm is the reduction of the four main craters (BN, VOR, NE and SE) to

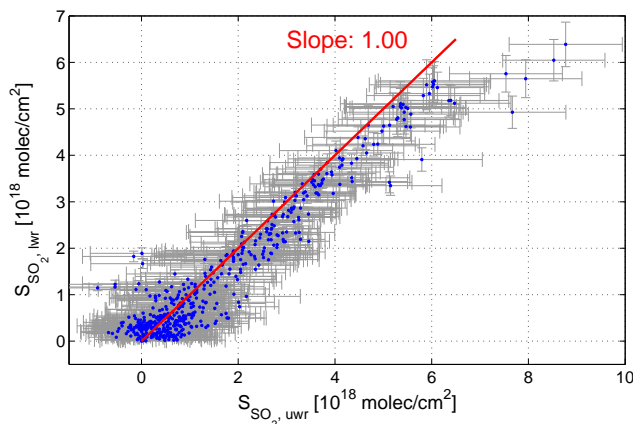


**Figure A3.** Retrieved SO<sub>2</sub> SCDs from the two SO<sub>2</sub> evaluation ranges. The evaluation scheme centred around 360 nm (SO<sub>2,uwr</sub>) is plotted on the  $x$  axis, while the scheme centred around 320 nm (SO<sub>2,lwr</sub>) is on the  $y$  axis. The red line indicates perfect correlation in both ranges. In the case of large SO<sub>2</sub> SCDs (i.e.  $S_{\text{SO}_2} > 3 \times 10^{18}$  molecules cm<sup>-2</sup>), the retrieved SCDs in the lwr-range are increasingly underestimated.

a single emission source point  $P_0$  (i.e.  $\tau = 0$  point) located at  $37^\circ 45' 6.7''$  N,  $14^\circ 59' 49.6''$  E between the central craters (BN, VOR) and NE.

Furthermore, chemical processes which may have already taken place within the craters are also not considered in our routine. The latter effect can cause a plume age offset with respect to  $P_0$ . Both effects are strongest for viewing directions close to the vent where the plumes are still separated. However, in most cases the corresponding error was assessed to be relatively small considering the uncertainties in the meteorological data.

#### A6 Correction algorithm for stratospheric BrO

The BrO SCDs ( $S_{\text{meas}}$ ) derived from the DOAS evaluation (see Sect. 3.4) are composed of a volcanic ( $S_{\text{plume}}$ ) and a stratospheric contribution ( $dS_{\text{str}}$ ). The latter is due to changes in the zenith angle ( $\Theta$ ) between plume spectrum and FRS.

$$S_{\text{plume}} = S_{\text{meas}} - dS_{\text{str}} \quad (\text{A2})$$

In order to examine  $dS_{\text{str}}$  we used a simple geometrical approach assuming that the stratospheric AMF  $X$  is given by  $X = \cos(\Theta)^{-1}$  (see also Hönninger et al., 2004). For our purposes, this assumption was assessed to be sufficient, since plume spectra and FRS were recorded close in time and the SZAs were in most cases (99.1 %) smaller than  $80^\circ$ . For a more accurate estimation of the AMF, radiative transfer calculations are necessary.

The AMF relates the stratospheric slant column  $S_{\text{str},i}$  of a given spectrum  $i$  to the corresponding vertical column  $V_{\text{str}}$ :  $S_{\text{str},i} = V_{\text{str}}/\cos(\Theta_i)$ . Based on this, the corresponding stratospheric contribution  $dS_{\text{str},ij}$  between two spectra  $i, j$

can be determined from the vertical column and the difference in the AMF:

$$dS_{\text{str},ij} = V_{\text{str}} \times \left( \frac{1}{\cos(\Theta_i)} - \frac{1}{\cos(\Theta_j)} \right) \stackrel{\text{def}}{=} V_{\text{str}} \times \gamma_{ij}. \quad (\text{A3})$$

Inserting Eq. (A3) into Eq. (A2) yields the following relation for the corresponding volcanic BrO column:

$$S_{\text{plume}} = S_{\text{meas}} - V_{\text{str,BrO}} \times \gamma_{ij}. \quad (\text{A4})$$

Following the results published by Sinnhuber et al. (2005) and Schofield et al. (2004) we assumed a constant stratospheric BrO column of  $V_{\text{str,BrO}} = 4.0 \times 10^{13}$  molecules  $\text{cm}^{-2}$  for our correction. Large diurnal variations in the stratospheric BrO column are unlikely for the SZA range covered by our data set ( $\Theta < 83^\circ$ ). Thus, all retrieved BrO columns were corrected using Eq. (A4). The relative percentage impact (i.e.  $dS_{\text{str}}/S_{\text{meas}}$ ) of stratospheric signals on our BrO retrieval is visualised in Fig. A4.

Of course, the relative impact of the stratospheric contribution increases for smaller (measured) BrO SCDs (compare e.g. dark blue with green colours in Fig. A4). For BrO SCDs of the order of  $6 \times 10^{14}$  molecules  $\text{cm}^{-2}$  (green colours) we found that the impact of  $dS_{\text{str}}$  on the measured signal amounts to  $a = 6.6\%/\gamma_{ij}$  (linear regression in Fig. A4).

In order to estimate the influence of potential variations in the total stratospheric BrO load ( $V_{\text{str,BrO}}$ ), we additionally determined this slope for two different stratospheric BrO VCDs of  $V_{\text{str,BrO}} = 2 \times 10^{13}$  and  $V_{\text{str,BrO}} = 7 \times 10^{13}$  molecules  $\text{cm}^{-2}$ .

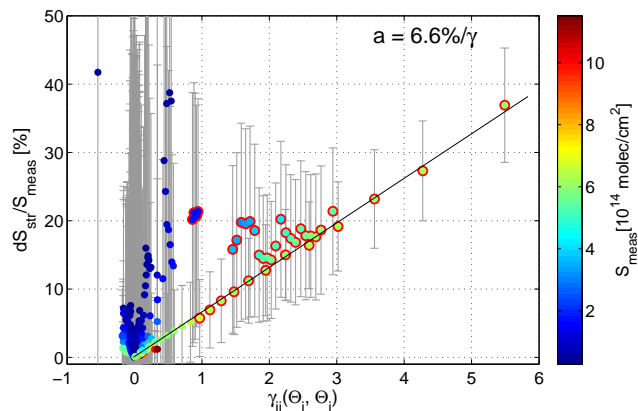


**Figure A4.** Relative deviation ( $dS_{\text{str}}/S_{\text{meas}}$ ) of volcanic BrO from the measured SCDs ( $S_{\text{meas}}$ , colour-coded) due to stratospheric BrO differential SCDs. We assumed a vertical stratospheric BrO column of  $V_{\text{str,BrO}} = 4.0 \times 10^{13}$  molecules  $\text{cm}^{-2}$ . The results are plotted as a function of  $\gamma_{ij}(\Theta_i, \Theta_j)$  (i.e.  $\Delta\text{SZA}$ , see Eq. A4). We included all spectra from our data set with significant BrO SCDs corresponding to the respective detection limit. For 8 % of the data, the stratospheric contribution ( $dS_{\text{str}}$ ) exceeded the corresponding fit error (marked with red circles). All of these cases were observed at  $\gamma_{ij}$  values exceeding 0.86; the corresponding measurements were performed before 08:15 or after 16:45 LT.

The corresponding impacts were  $a = 3.4\%/\gamma_{ij}$  and  $a = 11.8\%/\gamma_{ij}$  respectively. This shows that influences due to stratospheric BrO are in most cases relatively small (i.e. for small  $\gamma_{ij}$  values) even for considerably large stratospheric VCDs. Nonetheless, one has to keep in mind that these slopes were determined at considerably large BrO levels of the order of  $S_{\text{meas}} = 6 \times 10^{14}$  molecules  $\text{cm}^{-2}$ . For lower measured BrO SCDs (blue colours in Fig. A4) the impact of stratospheric BrO increases and can significantly influence the volcanic signal, especially at large differences in the SZA between plume spectrum and FRS (i.e. at large  $\gamma_{ij}$  values).

**Acknowledgements.** We like to thank Henning Finkenzeller, Marco Huwe and Constantin Mayer for helpful discussions and for their great help with preparing and conducting the field campaign at Mt. Etna. Parts of the data presented in this work were obtained during the “Etna – Pizzi Deneri field trip” organised and supported by the Università degli Studi di Palermo (DiSTeM) and the Istituto Nazionale di Geofisica e Vulcanologia (INGV) of Catania and Palermo. We would furthermore like to thank Evelyn Jäkel for the determination of the OCIO photolysis. We thank Udo Frieß for providing and further developing the software package MS-DOAS. Furthermore, we would like to thank Robert Holla, Johannes Zielcke, Stefan Schmidt, Martin Horbanski and Peter Lübcke for their great practical and theoretical support before and after the field campaign. We also thank the workshop crew of the Institute of Environmental Physics for their support in completing the instrument. J. Gliß and N. Bobrowski thank for the financial support from the DFG project “DFG BO 3611/1-1”. Furthermore, we wish to thank the Editor J. Ma and three anonymous referees for their comments and helpful suggestions during the review process.

Edited by: J. Ma

## References

- Aiuppa, A., Inguaggiato, S., McGonigle, A., O’Dwyer, M., Oppenheimer, C., Padgett, M., Rouwet, D., and Valenza, M.: H<sub>2</sub>S fluxes from Mt. Etna, Stromboli, and Vulcano (Italy) and implications for the sulfur budget at volcanoes, *Geochim. Cosmochim. Ac.*, 69, 1861–1871, doi:10.1016/j.gca.2004.09.018, 2005.
- Barrie, L. A., Bottenheim, J. W., Schnell, R. C., Crutzen, P. J., and Rasmussen, R. A.: Ozone destruction and photochemical reactions at polar sunrise in the lower Arctic atmosphere, *Nature*, 334, 138–141, doi:10.1038/334138a0, 1988.
- Beirle, S., Hörmann, C., Penning de Vries, M., Dörner, S., Kern, C., and Wagner, T.: Estimating the volcanic emission rate and atmospheric lifetime of SO<sub>2</sub> from space: a case study for Kīlauea volcano, Hawai‘i, *Atmos. Chem. Phys.*, 14, 8309–8322, doi:10.5194/acp-14-8309-2014, 2014.
- Birks, J. W., Shoemaker, B., Leck, T. J., Borders, R. A., and Hart, L. J.: Studies of reactions of importance in the stratosphere, II. Reactions involving chlorine nitrate and chlorine dioxide, *J. Chem. Phys.*, 66, 4591–4599, doi:10.1063/1.433716, 1977.
- Bobrowski, N. and Giuffrida, G.: Bromine monoxide/sulphur dioxide ratios in relation to volcanological observations at Mt. Etna 2006–2009, *Solid Earth*, 3, 433–445, doi:10.5194/se-3-433-2012, 2012.
- Bobrowski, N. and Platt, U.: SO<sub>2</sub>/BrO ratios studied in five volcanic plumes, *J. Volcanol. Geoth. Res.*, 166, 147–160, doi:10.1016/j.jvolgeores.2007.07.003, 2007.
- Bobrowski, N., Hönninger, G., Galle, B., and Platt, U.: Detection of bromine monoxide in a volcanic plume, *NATURE*, 423, 273–276, doi:10.1038/nature01625, 2003.
- Bobrowski, N., von Glasow, R., Aiuppa, A., Inguaggiato, S., Louban, I., Ibrahim, O. W., and Platt, U.: Reactive halogen chemistry in volcanic plumes, *J. Geophys. Res.-Atmos.*, 112, D06311, doi:10.1029/2006JD007206, 2007.
- Bobrowski, N., Kern, C., Platt, U., Hörmann, C., and Wagner, T.: Novel SO<sub>2</sub> spectral evaluation scheme using the 360–390 nm wavelength range, *Atmos. Meas. Tech.*, 3, 879–891, doi:10.5194/amt-3-879-2010, 2010.
- Bogumil, K., Orphal, J., Homann, T., Voigt, S., Spietz, P., Fleischmann, O., Vogel, A., Hartmann, M., Kromminga, H., Bovensmann, H., Frerick, J., and Burrows, J.: Measurements of molecular absorption spectra with the SCIAMACHY pre-flight model: instrument characterization and reference data for atmospheric remote-sensing in the 230–2380 nm region, *J. Photoch. Photobio. A*, 157, 167–184, doi:10.1016/S1010-6030(03)00062-5, 2003.
- Burrows, J., Richter, A., Dehn, A., Deters, B., Himmelmann, S., and Orphal, J.: Atmospheric remote-sensing reference data from GOME-2, temperature-dependent absorption cross sections of O<sub>3</sub> in the 231–794 nm range, *J. Quant. Spectrosc. Ra.*, 61, 509–517, doi:10.1016/S0022-4073(98)00037-5, 1999.
- Carroll, M. R. and Holloway, J. R.: Volatiles in magmas, *Mineralogical Society of America*, <http://www.minsocam.org/msa/rim/Rim30.html> (last access: 29 September 2014), ISBN 0-939950-36-7/ISBN13 978-0-939950-36-2, 517 pp., 1994.
- Chance, K. and Kurucz, R.: An improved high-resolution solar reference spectrum for earth’s atmosphere measurements in the ultraviolet, visible, and near infrared, *J. Quant. Spectrosc. Ra.*, 111, 1289–1295, doi:10.1016/j.jqsrt.2010.01.036, 2010.
- Donovan, A., Tsanev, V., Oppenheimer, C., and Edmonds, M.: Reactive halogens (BrO and OCIO) detected in the plume of Soufrière Hills Volcano during an eruption hiatus, *Geochem. Geophys. Geosy.*, 15, 3346–3363, doi:10.1002/2014GC005419, 2014.
- Fickert, S., Adams, J. W., and Crowley, J. N.: Activation of Br<sub>2</sub> and BrCl via uptake of HOBr onto aqueous salt solutions, *J. Geophys. Res.-Atmos.*, 104, 23719–23727, doi:10.1029/1999JD900359, 1999.
- Fleischmann, O. C., Meyer-Arnek, J., Burrows, J. P., and Orphal, J.: The Visible Absorption Spectrum of OBrO, Investigated by Fourier Transform Spectroscopy, *J. Phys. Chem. A*, 109, 5093–5103, doi:10.1021/jp044911x, 2005.
- Francis, P., Maciejewski, A., Oppenheimer, C., Chaffin, C., and Caltabiano, T.: SO<sub>2</sub> : HCl ratios in the plumes from Mt. Etna and Vulcano determined by Fourier Transform Spectroscopy, *Geophys. Res. Lett.*, 22, 1717–1720, doi:10.1029/95GL01657, 1995.
- General, S., Bobrowski, N., Pöhler, D., Weber, K., Fischer, C., and Platt, U.: Airborne I-DOAS measurements at Mt. Etna: BrO and OCIO evolution in the plume, *J. Volcanol. Geoth. Res.*, doi:10.1016/j.jvolgeores.2014.05.012, in press, 2015.
- Gerlach, T.: Volcanic sources of tropospheric ozone-depleting trace gases, *Geochem. Geophys. Geosy.*, 5, Q09007, doi:10.1029/2004GC000747, 2004.
- Greenblatt, G. D., Orlando, J. J., Burkholder, J. B., and Ravishankara, A. R.: Absorption measurements of oxygen between 330 and 1140 nm, *J. Geophys. Res.-Atmos.*, 95, 18577–18582, doi:10.1029/JD095iD11p18577, 1990.
- Hermans, C., A. C., V., Fally, S., Carleer, M., Colin, R., Coquart, B., Jenouvrier, A., and Merienne, M.-F.: Absorption cross-section of the collision-induced bands of oxygen from the UV to the NIR, *Proceedings of the NATO Advanced Research Workshop, Weakly Interacting Molecular Pairs: Unconventional Absorbers of Radiation in the Atmosphere*, France, 24 April–2 May 2002, NATO Science Series IV Earth and Environmental Sciences, 27, 193–202, available at: <http://www.aeronomie.be/spectrolab/o2.htm> (last access: 2 May 2015), 2003.

- Hermans, C., Vandaele, A., and Fally, S.: Fourier transform measurements of SO<sub>2</sub> absorption cross sections: I. Temperature dependence in the 24 000–29 000 cm<sup>-1</sup> (345–420 nm) region, *J. Quant. Spectrosc. Ra.*, 110, 756–765, doi:10.1016/j.jqsrt.2009.01.031, 2009.
- Hönninger, G., von Friedeburg, C., and Platt, U.: Multi axis differential optical absorption spectroscopy (MAX-DOAS), *Atmos. Chem. Phys.*, 4, 231–254, doi:10.5194/acp-4-231-2004, 2004.
- Hörmann, C., Sihler, H., Bobrowski, N., Beirle, S., Penning de Vries, M., Platt, U., and Wagner, T.: Systematic investigation of bromine monoxide in volcanic plumes from space by using the GOME-2 instrument, *Atmos. Chem. Phys.*, 13, 4749–4781, doi:10.5194/acp-13-4749-2013, 2013.
- Jaeschke, W., Berresheim, H., and Georgii, H.-W.: Sulfur emissions from Mt. Etna, *J. Geophys. Res.-Oceans*, 87, 7253–7261, doi:10.1029/JC087iC09p07253, 1982.
- Kalabokas, P. D., Cammas, J.-P., Thouret, V., Volz-Thomas, A., Boulanger, D., and Repapis, C. C.: Examination of the atmospheric conditions associated with high and low summer ozone levels in the lower troposphere over the eastern Mediterranean, *Atmos. Chem. Phys.*, 13, 10339–10352, doi:10.5194/acp-13-10339-2013, 2013.
- Kelly, P. J., Kern, C., Roberts, T. J., Lopez, T., Werner, C., and Aiuppa, A.: Rapid chemical evolution of tropospheric volcanic emissions from Redoubt Volcano, Alaska, based on observations of ozone and halogen-containing gases, the 2009 Eruption of Redoubt Volcano, Alaska, *J. Volcanol. Geoth. Res.*, 259, 317–333, doi:10.1016/j.jvolgeores.2012.04.023, 2013.
- Kern, C., Sihler, H., Vogel, L., Rivera, C., Herrera, M., and Platt, U.: Halogen oxide measurements at Masaya Volcano, Nicaragua using active long path differential optical absorption spectroscopy, *B. Volcanol.*, 71, 659–670, doi:10.1007/s00445-008-0252-8, 2009.
- Kern, C., Deutschmann, T., Vogel, L., Woehrbach, M., Wagner, T., and Platt, U.: Radiative transfer corrections for accurate spectroscopic measurements of volcanic gas emissions, *B. Volcanol.*, 72, 233–247, doi:10.1007/s00445-009-0313-7, 2010.
- Kern, C., Deutschmann, T., Werner, C., Sutton, A. J., Elias, T., and Kelly, P. J.: Improving the accuracy of SO<sub>2</sub> column densities and emission rates obtained from upward-looking UV-spectroscopic measurements of volcanic plumes by taking realistic radiative transfer into account, *J. Geophys. Res.-Atmos.*, 117, D20302, doi:10.1029/2012JD017936, 2012.
- Kraus, S.: DOASIS: A framework design for DOAS, Shaker, <http://books.google.no/books?id=GFF5AAAACAAJ> (last access: 25 September 2014), 2006.
- La Spina, A., Burton, M., and Salerno, G. G.: Unravelling the processes controlling gas emissions from the central and northeast craters of Mt. Etna, *J. Volcanol. Geoth. Res.*, 198, 368–376, doi:10.1016/j.jvolgeores.2010.09.018, 2010.
- Lee, C., Kim, Y. J., Tanimoto, H., Bobrowski, N., Platt, U., Mori, T., Yamamoto, K., and Hong, C. S.: High ClO and ozone depletion observed in the plume of Sakurajima volcano, Japan, *Geophys. Res. Lett.*, 32, L21809, doi:10.1029/2005GL023785, 2005.
- Lee, C., Martin, R. V., van Donkelaar, A., Lee, H., Dickerson, R. R., Hains, J. C., Krotkov, N., Richter, A., Vinnikov, K., and Schwab, J. J.: SO<sub>2</sub> emissions and lifetimes: estimates from inverse modeling using in situ and global, space-based (SCIAMACHY and OMI) observations, *J. Geophys. Res.-Atmos.*, 116, D06304, doi:10.1029/2010JD014758, 2011.
- Lehrer, E., Wagenbach, D., and Platt, U.: Aerosol chemical composition during tropospheric ozone depletion at Ny Alesund/Svalbard, *Tellus B*, 49, 486–495, doi:10.1034/j.1600-0889.49.issue5.5.x, 1997.
- Louban, I., Bobrowski, N., Rouwet, D., Inguaggiato, S., and Platt, U.: Imaging DOAS for volcanological applications, *B. Volcanol.*, 71, 753–765, doi:10.1007/s00445-008-0262-6, 2009.
- Lübcke, P., Bobrowski, N., Arellano, S., Galle, B., Garzón, G., Vogel, L., and Platt, U.: BrO/SO<sub>2</sub> molar ratios from scanning DOAS measurements in the NOVAC network, *Solid Earth*, 5, 409–424, doi:10.5194/se-5-409-2014, 2014.
- Martin, R., Mather, T., and Pyle, D.: High-temperature mixtures of magmatic and atmospheric gases, *Geochim. Geophys. Geos.*, 7, Q04006, doi:10.1029/2005GC001186, 2006.
- Martin, R. S., Mather, T. A., Pyle, D. M., Power, M., Allen, A. G., Aiuppa, A., Horwell, C. J., and Ward, E. P. W.: Composition-resolved size distributions of volcanic aerosols in the Mt. Etna plumes, *J. Geophys. Res.-Atmos.*, 113, D17211, doi:10.1029/2007JD009648, 2008.
- Mayer, B. and Kylling, A.: Technical note: The libRadtran software package for radiative transfer calculations – description and examples of use, *Atmos. Chem. Phys.*, 5, 1855–1877, doi:10.5194/acp-5-1855-2005, 2005.
- McGonigle, A. J. S., Delmelle, P., Oppenheimer, C., Tsanev, V. I., Delfosse, T., Williams-Jones, G., Horton, K., and Mather, T. A.: SO<sub>2</sub> depletion in tropospheric volcanic plumes, *Geophys. Res. Lett.*, 31, L13201, doi:10.1029/2004GL019990, 2004.
- Meller, R. and Moortgat, G.: Temperature dependence of the absorption cross sections of formaldehyde between 223 and 323 K in the wavelength range 225–375 nm, *J. Geophys. Res.-Atmos.*, 105, 7089–7101, doi:10.1029/1999JD901074, 2000.
- Mori, T., Mori, T., Kazahaya, K., Ohwada, M., Hirabayashi, J., and Yoshikawa, S.: Effect of UV scattering on SO<sub>2</sub> emission rate measurements, *Geophys. Res. Lett.*, 33, L17315, doi:10.1029/2006GL026285, 2006.
- Oppenheimer, C., Tsanev, V. I., Braban, C. F., Cox, R. A., Adams, J. W., Aiuppa, A., Bobrowski, N., Delmelle, P., Barclay, J., and McGonigle, A. J. S.: BrO formation in volcanic plumes, *Geochim. Cosmochim. Ac.*, 70, 2935–2941, doi:10.1016/j.gca.2006.04.001, 2006.
- Platt, U.: Reactive Halogen Species in the Mid-Latitude Troposphere – Recent Discoveries, *Water Air Soil Poll.*, 123, 229–244, doi:10.1023/A:1005267321567, 2000.
- Platt, U. and Janssen, C.: Observation and role of the free radicals NO<sub>3</sub>, ClO, BrO and IO in the troposphere, *Faraday Discuss.*, 100, 175–198, doi:10.1039/FD9950000175, 1995.
- Platt, U. and Stutz, J.: *Differential Optical Absorption Spectroscopy: Principles and Application*, Springer, doi:10.1007/978-3-540-75776-4, 2008.
- Pyle, D. and Mather, T.: Halogens in igneous processes and their fluxes to the atmosphere and oceans from volcanic activity: a review, *Chem. Geol.*, 263, 110–121, doi:10.1016/j.chemgeo.2008.11.013, 2009.
- Roberts, T., Braban, C., Martin, R., Oppenheimer, C., Adams, J., Cox, R., Jones, R., and Griffiths, P.: Modelling reactive halogen formation and ozone depletion in volcanic plumes, *Chem. Geol.*, 263, 151–163, doi:10.1029/JD095iD11p18577, 2009.

- Robock, A.: Volcanic eruptions and climate, *Rev. Geophys.*, 38, 191–219, doi:10.1029/1998RG000054, 2000.
- Sander, S. P., Friedl, R. R., Golden, D. M., Kurylo, M. J., Moortgat, G. K., Keller-Rudeck, H., Wine, P. H., Ravishankara, A. R., Kolb, C. E., Molina, M. J., Finlaysson-Pitts, B. J., Huie, R. E., and Orkin, R. L.: Chemical Kinetics and Photochemical Data for Use in Atmospheric Studies, Tech. Rep. Evaluation Number 15, JPL Publication, 06–2, Jet Propulsion Laboratory, NASA, available at: <http://jpldataeval.jpl.nasa.gov/> (last access: 2 May 2015), 2006.
- Schofield, R., Kreher, K., Connor, B. J., Johnston, P. V., Thomas, A., Shooter, D., Chipperfield, M. P., Rodgers, C. D., and Mount, G. H.: Retrieved tropospheric and stratospheric BrO columns over Lauder, New Zealand, *J. Geophys. Res.-Atmos.*, 109, D14304, doi:10.1029/2003JD004463, 2004.
- Simpson, W. R., von Glasow, R., Riedel, K., Anderson, P., Ariya, P., Bottenheim, J., Burrows, J., Carpenter, L. J., Frieß, U., Goodsite, M. E., Heard, D., Hutterli, M., Jacobi, H.-W., Kaleschke, L., Neff, B., Plane, J., Platt, U., Richter, A., Roscoe, H., Sander, R., Shepson, P., Sodeau, J., Steffen, A., Wagner, T., and Wolff, E.: Halogens and their role in polar boundary-layer ozone depletion, *Atmos. Chem. Phys.*, 7, 4375–4418, doi:10.5194/acp-7-4375-2007, 2007.
- Sinnhuber, B.-M., Rozanov, A., Sheode, N., Afe, O. T., Richter, A., Sinnhuber, M., Wittrock, F., Burrows, J. P., Stiller, G. P., von Clarmann, T., and Linden, A.: Global observations of stratospheric bromine monoxide from SCIAMACHY, *Geophys. Res. Lett.*, 32, L20810, doi:10.1029/2005GL023839, 2005.
- Spietz, P., Martín, J. C. G., and Burrows, J. P.: Spectroscopic studies of the I<sub>2</sub>O<sub>3</sub> photochemistry: Part 2. Improved spectra of iodine oxides and analysis of the IO absorption spectrum, *J. Photoch. Photobio. A*, 176, 50–67, doi:10.1016/j.jphotochem.2005.08.023, 2005.
- Stutz, J. and Platt, U.: Numerical analysis and estimation of the statistical error of differential optical absorption spectroscopy measurements with least-squares methods, *Appl. Opt.*, 35, 6041–6053, doi:10.1364/AO.35.006041, 1996.
- Textor, C., Graf, H.-F., C., T., and Robock, A.: Emissions from volcanoes, in: *Emissions of Atmospheric Trace Compounds*, edited by: Granier, C., Artaxo, P., and Reeves, C., 269–303, Klewer, Dordrecht, Netherlands, doi:10.1007/978-1-4020-2167-1\_7, 2004.
- Theys, N., De Smedt, I., Van Roozendaal, M., Froidevaux, L., Clarisse, L., and Hendrick, F.: First satellite detection of volcanic OCIO after the eruption of Puyehue-Cordón Caulle, *Geophys. Res. Lett.*, 41, 667–672, doi:10.1002/2013GL058416, 2014.
- Turner, D. B.: Workbook of atmospheric dispersion estimates, Office of Air Programs Pub. No. AP-26, Environmental Protection Agency, 1970.
- Vogel, L.: Volcanic plumes: Evaluation of spectroscopic measurements, early detection and bromine chemistry, PhD thesis, Combined Faculties for the Natural Sciences and for Mathematics, Ruperto Carola University of Heidelberg, Germany, available at: <http://archiv.ub.uni-heidelberg.de/volltextserver/13219/> (last access: 2 May 2015), 2011.
- Vogel, L., Sihler, H., Lampel, J., Wagner, T., and Platt, U.: Retrieval interval mapping: a tool to visualize the impact of the spectral retrieval range on differential optical absorption spectroscopy evaluations, *Atmos. Meas. Tech.*, 6, 275–299, doi:10.5194/amt-6-275-2013, 2013.
- Voigt, S., Orphal, J., and Burrows, J.: The temperature and pressure dependence of the absorption cross-sections of NO<sub>2</sub> in the 250–800 nm region measured by Fourier-transform spectroscopy, *J. Photoch. Photobio. A*, 149, 1–7, doi:10.1016/S1010-6030(01)00650-5, 2002.
- Voigt, C., Jessberger, P., Jurkat, T., Kaufmann, S., Baumann, R., Schlager, H., Bobrowski, N., Giuffrida, G., and Salerno, G.: Evolution of CO<sub>2</sub>, SO<sub>2</sub>, HCl, and HNO<sub>3</sub> in the volcanic plumes from Etna, *Geophys. Res. Lett.*, 41, 2196–2203, doi:10.1002/2013GL058974, 2014.
- von Glasow, R.: Atmospheric chemistry in volcanic plumes, *P. Natl. Acad. Sci. USA*, 107, 6594–6599, doi:10.1073/pnas.0913164107, 2010.
- von Glasow, R., Bobrowski, N., and Kern, C.: The effects of volcanic eruptions on atmospheric chemistry, *Chem. Geol.*, 263, 131–142, doi:10.1016/j.chemgeo.2008.08.020, 2009.
- Vountas, M., Roznaov, V., and Burrows, J.: Ring effect: Impact of rotational Raman scattering on radiative transfer in earth's atmosphere, *J. Quant. Spectrosc. Ra.*, 60, 943–961, doi:10.1016/S0022-4073(97)00186-6, 1998.
- Wagner, T., Beirle, S., and Deutschmann, T.: Three-dimensional simulation of the Ring effect in observations of scattered sun light using Monte Carlo radiative transfer models, *Atmos. Meas. Tech.*, 2, 113–124, doi:10.5194/amt-2-113-2009, 2009.
- Wennberg, P.: Atmospheric chemistry: bromine explosion, *Nature*, 397, 299–301, doi:10.1038/16805, 1999.
- Wilmouth, D. M., Hanisco, T. F., Donahue, N. M., and Anderson, J. G.: Fourier transform ultraviolet spectroscopy of the  $A^2\Pi_{(3/2)} \leftarrow X^2\Pi_{(3/2)}$  transition of BrO, *J. Phys. Chem. A*, 103, 8935–8945, doi:10.1021/jp991651o, 1999.
- Wittmer, J., Bobrowski, N., Liotta, M., Giuffrida, G., Calabrese, S., and Platt, U.: Active alkaline traps to determine acidic-gas ratios in volcanic plumes: Sampling techniques and analytical methods, *Geochem. Geophys. Geosy.*, 15, 2797–2820, doi:10.1002/2013GC005133, 2014.